2

Physical properties of simulated galaxies from varying input physics

Abstract

We investigate the baryonic properties, such as stellar mass, (specific) star formation rate, gas consumption time scale, and gas fraction, of haloes at redshift two using a large set of high-resolution cosmological simulations from the *OWLS* project. We vary the sub-grid models for radiative cooling, reionization, the pressure of the unresolved multiphase ISM, star formation, feedback from massive stars and AGN, as well as the cosmology, box size and numerical resolution. While reionization and metal-line cooling are important for low- and high-mass haloes, respectively, galactic winds driven by feedback from star formation and/or accreting black holes determine the main properties of galaxies. The star formation rate is regulated through the ejection of gas by galactic winds. The gas fraction, and thus the star formation rate, adjusts until the (time averaged) rate at which energy/momentum are injected is sufficient to balance the accretion, which is itself determined by cosmology and cooling. Consequently, the assumed star formation law affects the gas fractions, but not the star formation rates. The predictions are sensitive to variations in the sub-grid implementation of galactic outflows, even if the energy per unit stellar mass is fixed. Feedback becomes inefficient if the initial wind velocity falls below a minimum value that increases with the pressure of the ISM and hence with halo mass. In galaxies from which winds do not escape, the pile up of newly formed metals results in catastrophic cooling and strong star formation. Our results suggests that a wide range of stellar mass functions could be produced by varying the initial wind velocity and mass loading with halo mass. In fact, even without such tuning many of our models predict stellar mass functions that agree with the observations. Reproducing the high values of the observed specific star formation rate appears, however, to be more difficult. In particular, the efficient feedback required to reproduce the mass function results in much lower specific star formation rates than observed.

2.1 Introduction

The formation of structure in the dark component of the Universe is reasonably well established by means of high resolution gravitational N-body simulations (e.g. Springel et al., 2005). The large-scale structure statistics derived from these gravity-only simulations agree very well with observations. The formation and evolution of galaxies is, however, much less well understood. Modeling the baryonic component is much more difficult than simulating the dark matter due to the collisional nature of the gas and the wealth of phenomena that need to be taken into account (cooling, star formation, feedback, etc.).

There are two popular approaches to tackle this challenging task. In semi-analytic models, analytic descriptions of the behaviour of the baryonic component, as a function of the dark matter halo mass, merging history and environment, describe the evolution of gas and stars (e.g. Kauffmann et al., 1999; Somerville & Primack, 1999; Croton et al., 2006; De Lucia et al., 2006; Fontanot et al., 2006, 2007; Monaco et al., 2007; De Lucia & Blaizot, 2007; Somerville et al., 2008; Bower et al., 2008). The freedom to choose functional forms and parameter values combined with the ability to run large numbers of models, ensure that reproducing observations is usually within reach. While this approach has great advantages, such as the ability to make mock galaxy surveys that are sufficiently realistic to reveal observational biases, there are also significant drawbacks. The large number of parameters can make it difficult to identify the key physical processes. More importantly, the ability to reproduce observations with a model that uses unphysical functional forms or unrealistic parameter values to describe physical processes can easily result in erroneous conclusions and misplaced confidence.

The other approach is to follow both the dark matter and the baryonic components by direct simulation. While the dark matter is nearly always simulated using particles, the baryons can either be modeled with Eulerian methods (discretizing the volume in an (adaptive) grid, Ryu et al., 1990; Cen et al., 1990; Cen & Ostriker, 1992; Gnedin, 1995; Bryan & Norman, 1998; Teyssier, 2002; Gottlöber & Yepes, 2007) or using the Lagrangian approach also used for the dark matter (discretizing the mass using particles, e.g. Evrard, 1988; Hernquist & Katz, 1989; Thomas & Couchman, 1992; Steinmetz & Mueller, 1993; Couchman et al., 1995; Serna et al., 1996; Shapiro et al., 1996; Steinmetz, 1996; Katz et al., 1996; Tissera et al., 1997; Dave et al., 1997; Springel & Hernquist, 2003a,b; Oppenheimer & Davé, 2006; Davé & Oppenheimer, 2007; Oppenheimer & Davé, 2008; Schaye et al., 2010). Here, the freedom is limited to the parametrization of unresolved sub-grid processes, principally outflows driven by feedback from star formation. The high computational expense associated with full numerical simulations prevents thorough explorations of parameter space. Together with the reduced level of freedom,

this means that numerical simulations tend to be less successful in reproducing observations of galaxy populations than semi-analytic models. Compared with the semi-analytic method, the advantages of the simulation approach include the much reduced (though still present) risk of getting the right answers for the wrong reasons, the ability to ask more detailed questions due to the tremendous increase in resolution, and the fact that not only galaxies, but also the intergalactic medium is modeled.

As many processes related to the baryons are not (well) resolved by even the highest resolution simulations, they are dealt with in the so-called sub-grid models. Among these are radiative cooling (e.g. Sutherland & Dopita, 1993; Wiersma et al., 2009a), the temperature and pressure of the multiphase gas at high densities (in the rest of the paper loosely called 'the ISM') and the formation of stars (e.g. Katz et al., 1996; Springel & Hernquist, 2003a; Schaye & Dalla Vecchia, 2008), the energy and momentum fed back by these stars into the ISM/ICM/IGM (e.g. Springel & Hernquist, 2003a; Dalla Vecchia & Schaye, 2008), stellar mass loss (e.g. Tornatore et al., 2007; Wiersma et al., 2009b) and the growth of supermassive black holes and associated feedback processes (e.g. Sijacki & Springel, 2006; Sijacki et al., 2007; Booth & Schaye, 2009).

In this work, we will use large, cosmological, hydrodynamical simulations to investigate a number of basic baryonic properties of haloes, including the (specific) star formation rate, stellar mass, gas and baryon fraction. In this way we will get a handle on the physical processes that determine the properties of galaxies and on the importance of the freedom that arises from choosing particular sub-grid models. As reproducing observations is not our main goal at this stage, we have not attempted to fine-tune our models or to optimise the sub-grid implementations.

We make use of the large suite of smoothed particle hydrodynamics (SPH) simulations from the *OverWhelmingly Large Simulations* project *OWLS* (Schaye et al., 2010). The large variety of input physics in the different runs, as well as the possibility to study the detailed numerical convergence of the results, enables us to investigate properties of haloes and their relation to the physical and numerical parameters. In the sub-grid models the philosophy is taken to keep it as simple as possible, and where possible the parameters are calibrated by observations. In particular, we will test several implementations of galactic winds, we will investigate the importance of metal-line cooling, and we will vary the treatment of the unresolved, multiphase interstellar medium, the star formation laws, the cosmological parameters, the stellar initial mass function, and the reionisation history. One implementation of AGN feedback will also be compared to the other models (for a comparison of several AGN models in the context of the *OWLS* suite, see Booth & Schaye, 2009).

This work complements that of Schaye et al. (2010), where we introduced the

simulations and compared the cosmic star formation histories predicted by the various models. The global star formation rate can be decomposed into a dark matter halo mass function, which is determined by the cosmology, and the statistical distribution of the star formation rate as a function of halo mass. Here we will study the latter, which is astrophysically more relevant than the global star formation rate as it removes the main effect of cosmology (the mass function) and allows us to investigate how the various baryonic processes vary with mass. Whilst we will add a dimension to the work of Schaye et al. (2010) by investigating the dependence on mass, we will remove another one in order to keep the scope of the study manageable. Thus, we will limit ourselves to $z = 2$ and to the high-resolution series presented in Schaye et al. (2010) (these runs were halted at this redshift). To get further insight, we will study many more properties of galaxies than the star formation rate. We will also study the stellar mass function which, however, does depend on the cosmology.

The structure of this chapter is as follows. In Section 2.2 we will describe the main features of our reference simulation, which serves as the baseline for the comparison between models, we describe how we select galaxies and we give an overview of the results. We elaborate on the physics variations in the subsequent Sections, where we discuss variations of cosmology (Sect. 2.3), metal-line cooling (Sect. 2.4), reionization (Sect. 2.5), the equation of state for high-density gas (Sect. 2.6), the star formation law (Sect. 2.7), the stellar initial mass function (Sect. 2.8), supernova feedback (Sect. 2.9), and AGN feedback (Sect. 2.10). After reading Section 2.2, all the other section can be read or skipped, depending on the readers' interests. Section 2.11 summarizes the conclusions. In Appendix 2.11 we present the tests showing the numerical convergence of our simulations, while Appendix 2.11 shows that the amount of energy and momentum inserted in the winds in the momentum driven wind models of Section 2.9.4, which are themselves taken from Oppenheimer & Davé (2006, 2008), is higher than what is available from either SN explosions or radiation pressure.

2.2 Numerical techniques

For a detailed discussion of the full set of *OWLS* models we refer the reader to Schaye et al. (2010). Here we will briefly summarize the reference simulation, its relevant numerical properties and the we will make some general notes on the physical properties we will show in all subsequent sections, which describe variations of the sub-grid models.

Table 2.1: Overview of the cosmological parameters of WMAP3 (*OWLS* reference) and WMAP1 (as used in the Millennium Simulation). Symbols have their usual meaning.

	WMAP3	WMAP1
Ω_m	0.238	0.25
Ω_b	0.0418	0.045
Ω_Λ	0.762	0.75
σ_8	0.74	0.9
n	0.951	1.0
$h = H_0$ / (100 km s^{-1} Mpc^{-1})	0.73	0.73

2.2.1 OverWhelmingly Large Simulations

The simulations are performed with an extended version of the N-Body Tree/SPH code GADGET3 (last described in Springel, 2005) in periodic boxes of 25 and 100 comoving h^{-1}Mpc. There are 512^3 dark matter and equally many baryonic particles (which can be either collisionless 'stars' or collisional 'gas' particles). The particle mass of the highest resolution simulation under consideration (25 h^{-1}Mpc box size, 2×512^3 particles) is $8.68 \times 10^6\ M_\odot$ for dark matter and $1.85 \times 10^6\ M_\odot$ for baryons (initially, the baryonic particle masses change in the course of the simulation due to mass transfer from star particles to gas particles). The gravitational softening length initially is fixed in comoving coordinates at 1/25 the inter-particle spacing. Below $z = 2.91$ the softening is fixed in proper units, at 0.5 h^{-1}kpc.

Initial conditions are generated with CMBFAST (Seljak & Zaldarriaga, 1996) and evolved forward in time from an initial glass-like state using the Zel'Dovich (1970) approximation to $z = 127$, where the simulation is started. The cosmology assumed is summarized in Table 2.1 and is deduced from the WMAP 3 year results (Spergel et al., 2007). The results are largely consistent with the more recent WMAP5 results (Komatsu et al., 2009), the most notable difference is in σ_8, which is 1.6 σ lower in WMAP3 than in WMAP5. The primordial helium mass fraction is set to 0.248

As the subgrid model variation is the main power of the *OWLS* suite, we will now describe the parameters and subgrid models used in the reference simulations. The next sections will be devoted to descriptions of the variations of the sub-grid models and how the different input physics affects the resulting galaxy population.

In the simulation radiative cooling and heating are calculated element-by-element by explicitly following the 11 elements H, He, C, N, O, Ne, Mg, Si, S, Ca and Fe in the presence of the Cosmic Microwave Background and the Haardt & Madau (2001) model for the UV/X-ray background radiation from quasars and

galaxies, as described in Wiersma et al. (2009a). Note that the gas is assumed to be optically thin and in photo-ionization equilibrium.

At sufficiently high pressures, deep inside haloes, we expect the gas to be composed of several phases, ranging from hot/warm tenuous gas to cold, dense molecular clouds. This high density, multi-phase interstellar medium (ISM) is not resolved (and our simulations lack the physics to describe it). The formation of a cold phase and instabilities to form stars require a physical hydrogen number density of $n_{\rm H} > 10^{-1}$ cm^{-3} (Schaye, 2004) and particles with such densities are put on a polytropic effective equation of state (EoS). Their pressure $P \propto \rho^{\gamma_{\rm eff}}$, where $\gamma_{\rm eff}$ is the polytropic index and ρ is the physical proper mass density of the gas. We use $\gamma_{\rm eff} = 4/3$, such that both the Jeans mass and the ratio of the Jeans length and the SPH kernel are independent of the density, thus preventing spurious fragmentation due to a lack of numerical resolution (Schaye & Dalla Vecchia, 2008). The normalization of the polytropic equation of state is such that the energy per unit mass corresponds to 10^4 K for atomic gas with primordial abundances at the star formation threshold ($P/k = 1.08 \times 10^3$ K cm^{-3} for $n_{\rm H} = 10^{-1}$ cm^{-3}). Star formation is followed stochastically, with a pressure dependent star formation rate, obtained from the observed Kennicutt-Schmidt law (Kennicutt, 1998a) and local hydrostatic equilibrium, as discussed in Schaye & Dalla Vecchia (2008). Gas particles are only allowed to form stars when they are on the EoS, so there is a threshold density for star formation of $n_{\rm H} > 10^{-1}$ cm^{-3}.

The mass loss of the gas by AGB stars and by Type Ia and Type II (including Type Ib,c) supernovae is followed explicitly for the 11 elements needed for the cooling, as described in Wiersma et al. (2009b). The star particles are assumed to be simple stellar populations (SSPs) with a Chabrier (2003) initial mass function (IMF). The energy feedback from massive stars and supernovae is implemented kinetically, giving a number of SPH neighbours of newly formed stars a kick with a velocity of 600 km s^{-1}. The number of particles receiving such a kick is set by the dimensionless mass loading factor η, which is the amount of mass kicked in the wind per unit solar mass of stars formed. We use $\eta = 2$, which together with the chosen velocity corresponds to about 40% of the energy available from supernovae of type II (including Ib,c), for our assumed Chabrier (2003) IMF. For details on the kinetic wind implementation, see Dalla Vecchia & Schaye (2008).

2.2.2 Halo identification

Haloes are identified using a Friends-of-Friends (FoF) algorithm, linking together all dark matter particles which are closer to each other than the linking parameter ($b = 0.2$ times the mean inter-particle distance). FoF identifies iso-overdensity contours of $\delta \equiv (\rho - \overline{\rho})/\overline{\rho} \simeq 3/(2\pi b^3) \simeq 60$ (Lacey & Cole, 1994). Outside these

contours, due to particle noise, some regions will also be selected as haloes. These haloes will be excluded by the particle number cuts we will make further on, as motivated by the convergence tests. Baryonic particles are linked to their nearest dark matter particle and belong to the same group, if any.

Following the convergence tests presented in Appendix 2.11, we only include haloes that contain at least 100 star particles when looking at halo properties as a function of stellar mass. We use a minimum of 2000 dark matter particles when we plot properties against halo mass. These two cuts produce nearly identical halo samples in the reference simulation and ensure that only well resolved haloes are considered.

Whenever we show the correlation between two halo properties, the plot consists of lines that connect the medians of bins, evenly spaced in the quantity plotted along the horizontal axis, if there are at least 30 points in that bin. If not, then the next bin extends to include the first next 30 objects. The last bin may contain between 0 and 30 objects. We bin the data starting from the high mass end. There, the difference in mass for two consecutive haloes is much bigger than at the low mass end, and in this way we are sure that the value of the mass at the high mass end of the plots is always the mean of the mass of the 15th and 16th most massive systems.

2.2.3 Physical properties

In subsequent sections we will study the relations between several physical properties of haloes. Simulations will be compared in sets that vary in only one aspect (e.g. only varying supernova feedback, or only varying the physics related to high density gas and star formation). The reference model (denoted *REF* and described in Sect. 2.2.1) will always be plotted as a black solid line, in order to intercompare the sets. The *REF* model serves as a baseline for our exploration of parameter space, but it should not be regarded as our 'best model'. For a more detailed description of the physics in the simulations we refer to Paper I. We will keep to the same order of model variations in Paper I for easy comparison. All sections will start with a summary of the models which should be sufficient to understand the discussion, but for more details we refer the reader to Paper I.

A graphical representation of the gas density of a galaxy formed in a representative set of models is shown in Fig. 2.2.2. The galaxy resides in a halo of total mass $\sim 10^{12.5}\ M_{\odot}$. It was first identified in the '*REF*' simulation, where its position (centre of mass of all particles within 10% of the virial radius) is determined. The line of sight is along the z-axis, which is almost perfectly aligned with the angular momentum vector of the gas within 10% of the virial radius ($\cos(\phi) = 0.994$). For the other simulations the image is centered on the same position, showing the re-

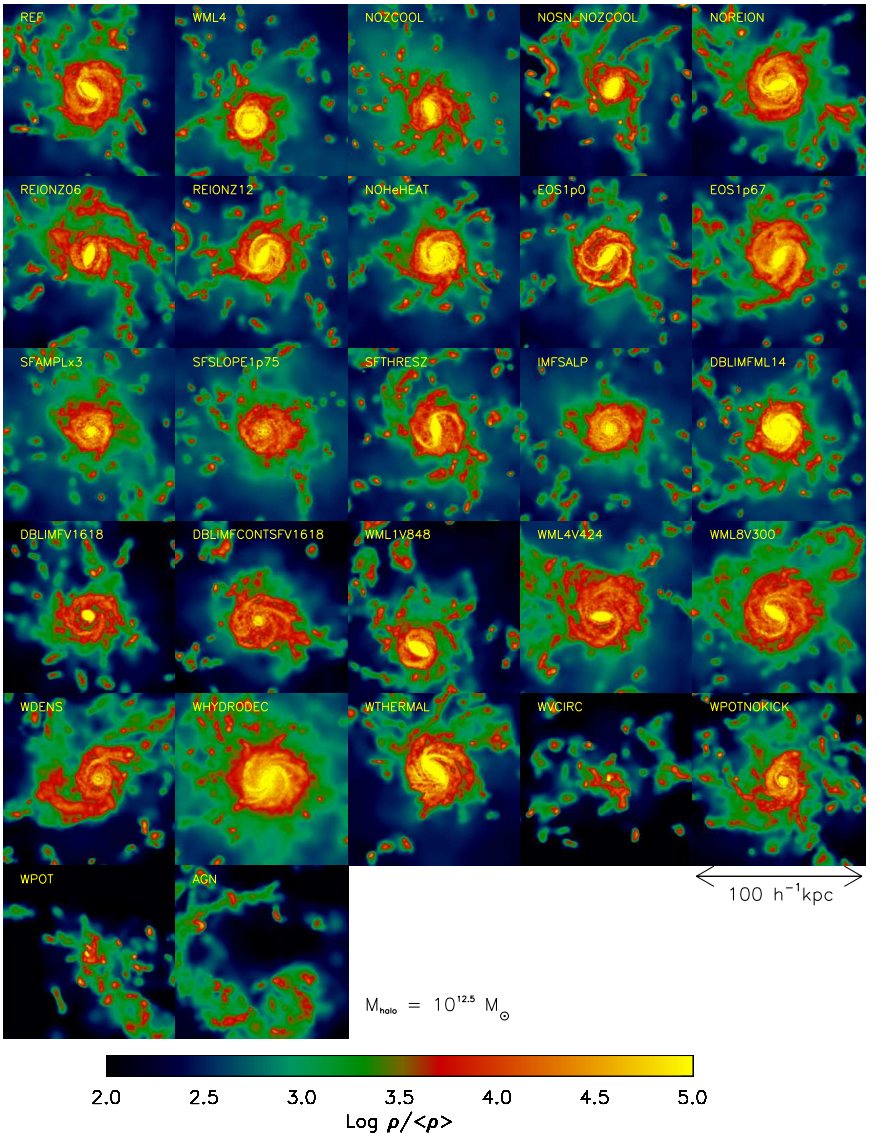

Figure 2.1: A graphical representation of a galaxy in a halo of $10^{12.5}$ $M_{\odot}$ in 20 of our simulations at redshift 2. The colour coding denotes the gas density divided by the mean density of the universe. All frames are 100 comoving kpc/h on a side and are centered on the position of the galaxy in the '*REF*' simulation. The gas density in a 100 comoving kpc/h box is projected. The orientation of the line of sight is along the z-axis, which is almost perfectly aligned with the angular momentum vector of all material inside 10% of the virial radius of this galaxy in the '*REF*' simulation.

markable similarity in the positions and orientations of the galaxies. The '*MILL*' simulation, as described below, was run with another cosmology, resulting in a different distribution of galaxies over the volume. This model was therefore left out.

In Fig. 2.2 we include all physics variations and plot 9 combinations of physical properties. The black line is the reference model from which we vary the input physics. In subsequent sections we will discuss sets of simulations which vary the input physics in some specific way. The upper two rows have halo mass on the horizontal axis, while the lower three panels show some properties as a function of stellar mass. Note that the upper six and lower three panels obey different resolution limits, as explained in Appendix 2.11. Fig. 2.2 shows the reference model in black and all other simulations in grey, such as to provide an idea of how much the different relations diverge in the different models. The remainder of this section gives some background on the panels where necessary. For every set of physical properties that will be discussed in the following sections we will use the same panels.

2.2.4 Properties as a function of halo mass

Panel (A) shows the stellar mass as a function of halo mass, which mainly serves as a way to connect the panels that have halo mass on the horizontal axis (A – F), to panels that have stellar mass on the horizontal axis (G – I). Panel (F) shows the stellar mass fraction of haloes as a function of their total mass and contains the same information. Dividing by the halo mass, though, emphasizes the differences between the models, because the stellar mass and total mass are tightly (and almost linearly) correlated.

In panel (B) we show the star formation rate of haloes as a function of their total mass. As we show in Fig. 2.2 the SFRs span slightly more than an order of magnitude at the high halo mass end, and less than an order of magnitude at the low mass end (except for the simulation without feedback and metal-line cooling). At the high mass end, the simulations with weak feedback (as described in Section 2.9) are the ones with the highest SFR, while the simulations showing a low SFR have either very efficient SN feedback, or AGN feedback.

In all panels (C) we plot the baryon fractions of the halo as a function of halo mass. We over-plot the universal baryon fraction (Ω_b/Ω_m), as appropriate for our default cosmology. Without feedback and metal-line cooling (which we will show separately in Fig. 2.4), the baryon fraction is very high, at around the universal value. Effective feedback sets the fractions well below the universal value, by factors up to 6 below it as can be seen in Fig. 2.2.

Most of our simulations show baryon fractions that are lower, and depend more

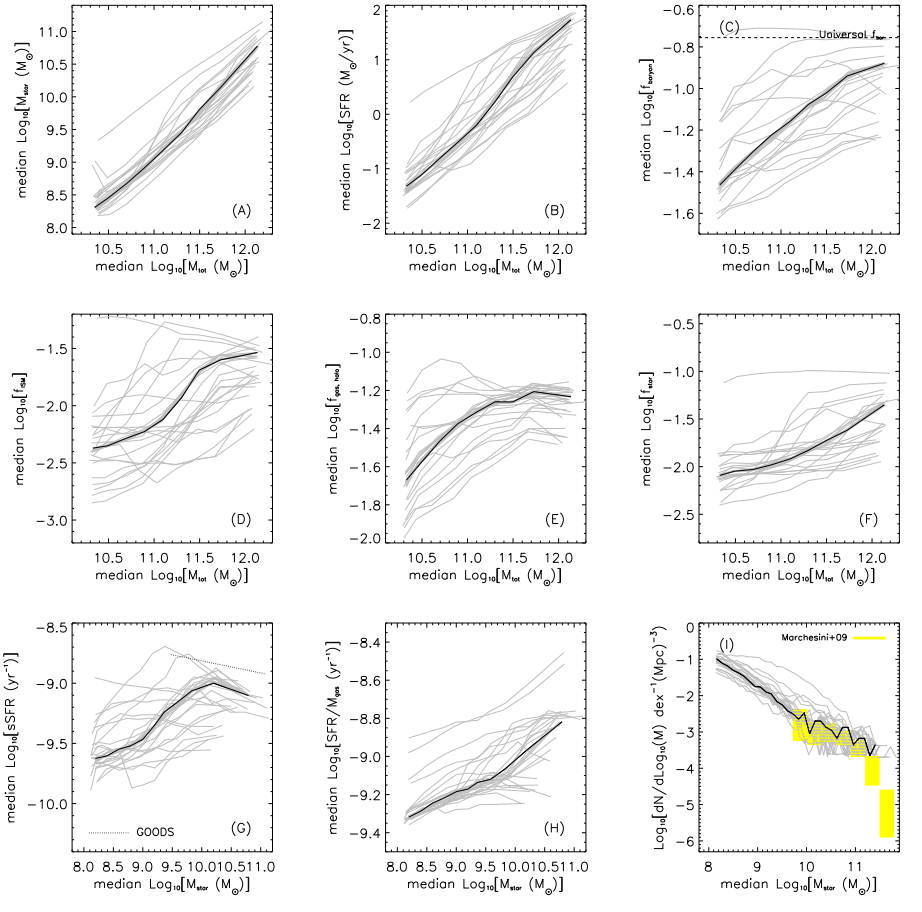

Figure 2.2: Median relations between halo properties in all the simulations described in this work. The reference model is shown in black and all other models are shown in grey. In subsequent sections we will consider sets of simulations in more detail. On the top two rows we show the halo mass as a function of stellar mass (panel A), star formation rate (panel B), baryon mass fraction (panel C), fraction of mass in the ISM (panel D), fraction of mass in other gas in the halo (panel E) and stellar mass fraction (panel F). The last three (second row) and up to the total baryonic mass fraction shown in panel (C). The last row shows stellar mass versus specific star formation rate (panel G), inverse of the gas consumption time scale (panel H) and the number density (the stellar mass function, panel I). We show medians in bins along the horizontal axes as described in the text for all haloes that satisfy the convergence criteria that apply to that specific panel.

strongly on mass, than those found by Crain et al. (2007). Those simulations included no cooling, no star formation and no feedback processes, making the results hard to compare directly. Our simulation without cooling and without feedback has a baryon fraction that goes above the universal value, whereas Crain et al. (2007) always stays below, at roughly 90% (unless the gas is preheated, then they do find a strong evolution with mass, as we do). Note, though, that we *do* include cooling from hydrogen and helium and star formation, whereas Crain et al. (2007) do not.

Panels (D) and (E) show the fraction of the mass that is in gas in the ISM and the rest of the gas in the haloes, respectively. In general, both are increasing functions of the total mass, although again some of the very inefficient feedback models show very high gas mass fractions in low mass haloes.

In the panels (F) we will look into the stellar mass fractions of haloes (the sum of the middle row panels, A through F, gives the upper right panel, C). As it will turn out, the stellar mass fractions tell us how well star formation is suppressed by the feedback model under consideration, whereas the baryon fractions of the haloes show a distinction between feedback models which remove gas from the ISM and models that remove the gas from the halo altogether.

2.2.5 Properties as a function of stellar mass

The integral of the SFR over time until the moment under consideration ($z = 2$ in this case) gives a stellar mass. Relations between SFR and stellar mass are not so well converged as those with halo mass (see Appendix 2.11). In higher resolution simulations the stellar mass that builds up is higher, because the star formation is well resolved already at earlier epochs (under-resolved star formation underestimates the SFR). The relations between stellar mass and SFR are very similar to the relations between halo mass and star formation rates (we do not show them). One notable difference occurs between the simulations without feedback and metal-line cooling. The much higher SFR in the simulation without feedback has resulted in the build-up of galaxies with very high stellar masses.

The specific star formation rate

An often used observational parameter is the specific star formation rate (sSFR), defined as the star formation rate divided by stellar mass. It basically is the inverse of the time needed to form the current stellar population with the current star formation rate. As colours of galaxies mainly measure the relative fraction of old to young stars (due to the different spectral regimes they shine in), the colour of a galaxy usually is a good measure of its sSFR (averaged over the recent past). In many previous studies the sSFR is used to distinguish starbursts from quiescently

star forming galaxies (comparing the sSFR to some other time scale, usually the Hubble time).

A good reason to look at sSFR instead of SFR is the almost linear relationship between stellar mass of haloes and their SFR, as we will show below. Dividing out the stellar mass removes the linear dependence and highlights deviations from this relation. Note that in a plot of sSFR against stellar mass there is no more information than in the plot of SFR against stellar mass.

The observations we will compare to are taken from Daddi et al. (2007), who measured the obscured and unobscured star formation by taking SFRs from the UV and IR together. They did this for *K*-selected *sBzK* galaxies (star forming, see Daddi et al., 2004) in the GOODS fields at $z \sim 2$. The median of the SFR as a function of stellar mass is well fit by SFR = $250 \cdot (M_*/10^{11}\ M_\odot)^{0.9}$, and the scatter is constant at about 0.2 dex. The scatter is not shown in the Figure, but is similar, although a bit smaller ($\sim$ 0.1 to 0.15 dex) in the simulations. Both the stellar masses and the star formation rates need to be converted to our cosmology and IMF, as explained in Sect. 2.2.5. The (cosmology and IMF corrected, see below) data from the GOODS fields of Daddi et al. (2007) have been transformed to sSFR instead of SFR. We plot the observed relation only on the mass range that actually is observed: $5 \times 10^9\ M_\odot < M_{\rm star} < 2 \times 10^{11}\ M_\odot$. Halo mass is much harder to observe than stellar mass and/or SFR (which usually come from SED modeling). Therefore we only show the specific star formation rate as a function of stellar mass.

As can be seen from panel (G) of Fig. 2.2 the medians of the sSFR of haloes span only a limited dynamic range of about an order of magnitude and are all lower than the observed relation, except for a very small range of stellar masses in simulations with inefficient feedback at these masses (see Section 2.9).

The slope in the relation between stellar mass and the specific star formation rate of a galaxy seem only to agree with the observations of Daddi et al. (2007) on mass ranges where the feedback is inefficient (either in simulations without feedback, or in the high mass haloes of simulations with relatively low wind velocities) and in the simulation with thermal supernova feedback. In simulations with ineffective feedback the slope in the sSFR$-M_*$ relation is negative, and even steeper than in the observations, while the simulation without feedback (and without metal-line cooling) shows a very similar slope to observations over a large range of masses (panel (G) of Fig. 2.4). The difference in normalization between the observations and our simulations may be due to the stellar masses in the simulations being too low (as star formation is only resolved at relatively low redshift), by the simulated star formation rates being too low or by the observed SFRs being too high. Besides, there may be systematics in the observations as well.

In the simulations with very strong feedback, either due to high wind veloci-

ties or to the inclusion of AGN, the specific star formation rates tend to become relatively independent of stellar mass. For these strong feedback models, the discrepancy in normalization between the observed and simulated star formation rates at given stellar mass are largest, though.

The agreement between observations and simulations without effective feedback in the slope of the relation is at odds with common tendency to invoke very effective stellar feedback in low mass haloes in semi-analytic models (e.g. Cole et al., 1994; Somerville & Primack, 1999; Cole et al., 2000; De Lucia et al., 2004) and simulations (e.g. Katz et al., 1996; Springel & Hernquist, 2003a) in order to fit the faint end of the luminosity function of galaxies in the local universe .

The gas consumption time scale

As star formation is expected to be more strongly influenced by the amount of available gas than by the amount of stars already formed, we define a second type of specific star formation rate, now normalizing the SFR by the mass in star forming gas. This is the inverse of the time needed to convert the present reservoir of star forming gas (i.e. gas that is on the equation of state) into stars with the present star formation rate, i.e. the inverse of the 'gas consumption time scale'. We plot the inverse of the gas consumption time scale as a function of stellar mass in panel(H).

Comparing simulations to observations

To correct observationally inferred stellar masses and SFRs from the cosmology assumed in the literature to our cosmology, we multiply them by the square of the ratio of luminosity distances $[d_{L,\text{our cosm}}(z)/d_{L,\text{obs cosm}}(z)]$. The subscripts 'our cosm' and 'obs cosm' denote our cosmology and the cosmology under which the observations are transformed into masses/SFRs, respectively.

The IMF assumed for the observations of the SFR we will compare our simulations to was the Salpeter (1955) IMF, whereas our stellar masses and SFRs are based on the Chabrier (2003) IMF. We therefore divide the observationally inferred SFRs by a factor 1.65, which is the asymptotic (reached after only 10^8 yr) ratio of the number of ionizing photons predicted by Bruzual & Charlot (2003) for a constant star formation rate. For comparison, the correction factor is $\sim$7 for the top-heavy IMFs used in starburst models (see Sect. 2.8.2). This top-heavy IMF is, however, really extreme.

For stellar masses, the IMF conversion factor is more sensitive to the age of the population and the observed rest-frame wavelength. As the light in most wavelength bands is dominated by massive stars and the high mass end of both the Salpeter and Chabrier IMFs are power laws with very similar power law indices,

we use the same factor of 1.65 as we used for the SFRs. For very old populations observed in red wavelength bands (tracing stellar continua, rather than dust emission) the conversion factor should be different. We verified that the K-band mass-to-light ratio is about a factor 1.65 smaller for a Chabrier than for a Salpeter IMF for SSPs and constantly star forming populations, for the full range of ages and metallicities available in the Bruzual & Charlot (2003) population synthesis package. We therefore also divide by a factor of 1.65 to convert stellar masses from the Salpeter to the Chabrier IMF.

In all panels (I) we will look at the number densities of galaxies as a function of their present day stellar mass at redshift 2. We bin the galaxies in 30 equally spaced bins in $\log M_*$, between the lowest resolved halo mass (containing 100 star particles, as the convergence tests allow us, see Appendix 2.11) and the highest available stellar mass in the simulation. The resulting stellar mass functions (MFs) are shown in panels (I). Over-plotted is an observed MF from a combined sample, using the deep near-infrared Multi-wavelength Survey by Yale-Chile, the Faint Infrared Extragalactic Survey and the Great Observatories Origins Deep Survey-Chandra Deep Field South surveys, as presented by Marchesini et al. (2009), also at $z = 2$.

In their paper, Marchesini et al. (2009) do a careful job in investigating all kinds of random and systematic errors. Here, we compare to their $1/V_{max}$ method results, including all uncertainties, but we leave out the bottom-light IMFs that they test. The reason for this is that they dominate the systematic errors and are more extreme assumptions than the variations in the other quantities. Also, for bottom-light IMFs there are only arguments at high redshift (Davé, 2008; van Dokkum, 2008; Wilkins et al., 2008a), and the interpretation of the observations are full of uncertainties themselves. The sources of random errors include poisson errors on the number counts, cosmic variance and the random errors from the use of photometric redshifts. These random errors are added in quadrature. To these random errors we linearly add the maximum of the systematic errors in the same mass bin, as Marchesini et al. (2009) did. The systematic errors include the systematic component in the errors from photometric redshifts, errors arising from different population synthesis packages (they test for Bruzual & Charlot, 2003; Maraston, 2005; Charlot & Bruzual, 2009) varying the metallicities of the stellar populations and the use of different extinction curves (Milky Way from Allen 1976, SMC from Prevot et al. 1984; Bouchet et al. 1985 Calzetti et al. 2000).

The correction factor for the IMF is very small, as the IMF used in the observational study is a diet Kroupa IMF. From Marchesini et al. (2009) we take the correction factor from Salpeter to the diet Kroupa: 1.6. With the factor between Salpeter and Chabrier (our IMF) of 1.65, the correction factor for stellar masses here is $1.65/1.6 = 1.03$ (diet Kroupa being slightly more massive for the same

observed luminosity). As this number is also derived from population synthesis packages, which come along with their own uncertainties we chose not to convert masses for the difference in IMFs. We do correct the masses for the difference in luminosity distances as described earlier. Number densities also need to be converted, as the volume at a given redshift is different for different angular diameter and comoving distances. Therefore, the number density (ϕ_*) is corrected for the ratio of volume elements (at the redshift under consideration, it is a function of the cosmological parameters given in Table 2.1). All numbers are given in natural units, without factors of the Hubble parameter, just as in Marchesini et al. (2009).

The resulting $1/V_{max}$ estimate of the analysis of Marchesini et al. (2009) is shown in the yellow shaded regions in all panels (I). We interpolated their values, as $z = 2$ is exactly on the boundary between two of their redshift bins ($1.3 < z < 2$ and $2 < z < 3$, respectively). We weigh the averaging to the sizes of the redshift intervals (weight 1.2 and 0.8 respectively), which results in parameters very consistent with $z = 2$ results of the Newfirm Medium-Band Survey (Marchesini et al. 2010, in prep.). The mass bins are not exactly the same in both redshift intervals either. The difference is very small. The upper mass limit of the most massive bin is the same and they use bins which are constant in $\log(M)$, of size 0.3 dex (at $1.3 < z < 2$) and 0.29 dex (at $2 < z < 3$), resulting in a difference of bin centre in the lowest mass bin 0.055 dex. We interpolate the mass bins in the same way as the errors, although using just either the low or high redshift mass bins instead would not make a noticeable difference. Note that we plot the logarithm of the number of galaxies per unit $\log M_*$, per unit volume.

As can be seen from panel (I) of Fig. 2.2 our mass functions fall well within the observed range, when all uncertainties are taken into account. This is true for a large sub-set of simulations, except some of the strongest feedback models (like the double IMF models in Fig. 2.9, the high constant wind velocity of Fig. 2.10, some of the momentum-driven wind models in Fig. 2.14 and AGN feedback in Fig. 2.15), which have too few very massive systems. Some very weak feedback models produce too many massive systems. At low masses it needs to be noted that our simulations go steeper than most faint end slopes of derived Schechter function parametrizations, but that this is largely outside the observed range of stellar masses.

Combining the results in panels (B) and (I) shows an interesting behaviour of the simulations: although the SFR is too low by a factor of a few, as compared to observations, we do form enough galaxies of all masses (and possibly too many low mass systems). A similar discrepancy, which may be related to the one highlighted here, is indicated by the works of Hopkins & Beacom (2006); Wilkins et al. (2008b), where they show that there is an internal discrepancy in measurements of the star formation rate density evolution and the build up of stellar mass density.

They conclude that the integral of the star formation rate results in a higher stellar mass than observed nowadays. One of many solutions is a possible overestimate of SFRs by a factor of a few. This would bring the observations and our simulations to much better agreement. See also Schaye et al. (2010) for a discussion on the integrated star formation properties of the simulations presented here.

2.3 Cosmology

Fig. 2.3

In order to investigate the dependence of the galaxy properties on cosmology, and to facilitate comparisons to earlier work, we vary the cosmology from the WMAP 3-year results (Spergel et al., 2007) to the so-called 'concordance cosmology' that was used in many previous studies including the Millennium Simulation (Springel et al., 2005). We will refer to this set of cosmological parameters as the 'Millennium cosmology' and denote the model assuming this cosmology '*MILL*'.

The main differences in the cosmologies is the value of σ_8, which is 0.74 in our reference cosmology, but 0.9 in the other model, and the universal baryon fraction Ω_b which is 0.0418 in all our simulations, except in the '*MILL*' simulation where it is 0.045. Other parameters are summarized in Table 2.1. In order to roughly match the peak in the observed global integrated star formation history the simulations with Millennium cosmology used a mass loading of $\eta = 4$ for the winds, rather than the $\eta = 2$ used in the reference model (Schaye et al., 2010). To isolate the effect of cosmology, we therefore compare it to a simulation with our default cosmology, but with a mass loading of $\eta = 4$ ('*WML4*'), which then corresponds to about 80% of the available energy from SNe. In Fig. 2.3 the effect of the cosmology can be addressed by comparing the blue dashed and red dotted line, which correspond to the WMAP3 and WMAP1 ('Millennium') cosmological parameters (as indicated in Table 2.1), respectively.

σ_8 basically sets the time scale for structure formation: a higher σ_8 corresponds to earlier structure formation (e.g. Peebles, 1993). As the concentration at a given mass is set by formation time, SFRs could be influenced by the value of σ_8, through different central densities. The two runs with different cosmologies (the red dotted and blue dashed line) assume the same wind energy per unit stellar mass (twice the energy assumed in the reference model, so 80% of the available supernova energy). The SFR of high mass haloes is slightly higher for the WMAP1 cosmology than for the WMAP3 cosmology, due to the different central densities at given mass, even if the feedback energy is the same. The much larger difference in the integrated star formation rate density of the universe, shown in Paper I is largely the effect of a different halo mass function at the same redshift. The larger number of haloes

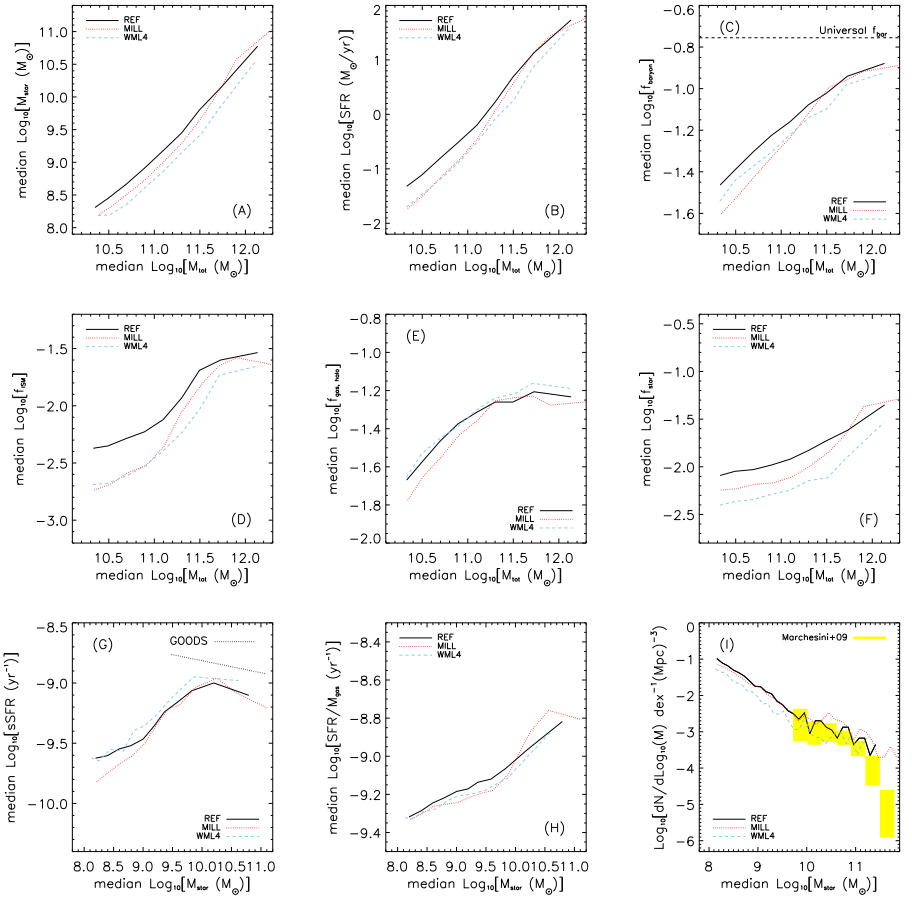

Figure 2.3: Like Fig. 2.2, but now only for a set of simulations in which the cosmology is varied from the WMAP three-year results, as in the reference model (black solid line), to the cosmology from the WMAP first year results (red dotted line), as they are used in the Millennium simulation. In the *'MILL'* simulation the supernova feedback was implemented with a two times higher mass loading in the winds, so two times more energy in the winds. The *'WML4'* (blue dashed line) run has the same cosmology as the reference model, but the same feedback as the *'MILL'* model, so for the effect of the cosmology the red dotted line should be compared to the blue dashed, while a comparison of the black solid and the blue dashed line shows the effect of increasing the wind mass loading with a factor of two.

results in a much higher global SFR density for the model with higher σ_8.

In the Millennium cosmology, the halo mass function is slightly higher than in our cosmology. This also holds for the stellar mass function, as shown in panel (I) and from panel (F) we learn that the stellar mass fraction as a function of halo mass is also higher (for models with the same feedback).

2.4 Metal-line cooling

Fig. 2.4

In this set of simulations we investigate what the effect is of cooling by metal lines. Simulations without any metal-line cooling are mostly affected in terms of gas cooling from temperatures of $\sim 10^{5-6}$ K, where the line cooling by metals is relatively efficient (e.g. Wiersma et al., 2009a). If gas shock heats to high temperatures while accreting onto galaxies, ignoring metal-line cooling will make it harder to cool down sufficiently to make it onto our artificial equation of state (see Section 2.6), where it is able to form stars. Metal-line cooling was turned off in the '*NOZCOOL*' models. A galaxy formed in these models can be seen in Fig. 2.2.2. Turning off metal-line cooling reduced the extent of the gaseous disk in this massive system, as cooling the gas at high temperatures in the halo is less efficient.

Comparing the red dotted with the black solid curve (the reference model) in panel (B) of Fig. 2.4 shows the effect of metal-line cooling on the star formation rates of galaxies. In general, metal-line cooling increases the SFR, because cooling rates increase with increasing metallicities (e.g. Cox & Tucker, 1969; Sutherland & Dopita, 1993; Wiersma et al., 2009a). This difference increases with halo mass, because the fraction of gas that is accreted hot and the halo virial temperature both increase with mass. The cooling is more and more affected by metals (the cooling rates of heavier elements have a peak at higher temperatures) for haloes of higher mass and higher virial temperature.

The mass fraction in ISM gas, as shown in panel (D) of Fig. 2.4 also shows that the fraction of 'cold' ISM gas is drastically lower for high mass haloes without feedback, than with feedback. For the higher halo masses, for which the feedback is inefficient (see Section. 2.9), there is a difference in gas consumption time scales, as can be seen in panel (H): star formation is more efficient in the models with metal-line cooling than in the models without. For low stellar masses, the winds (and thus the newly created metals) easily escape the galaxy, such that the difference in gas consumption time scale vanishes.

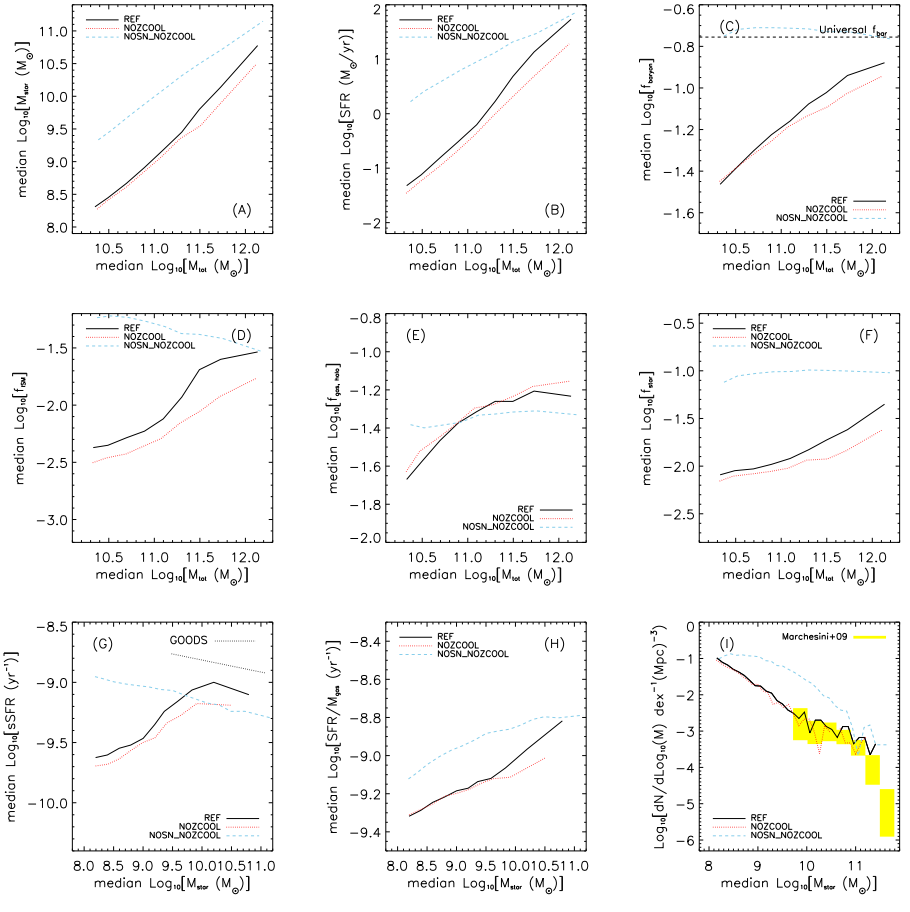

Figure 2.4: Like Fig. 2.2, but now only for a set of simulations in which the metal line cooling an/or the kinetic supernova feedback are turned off. The red dotted line shows the effect of turning of only metal line cooling, compared to the black line which shows the reference model. Turning off metal-line cooling and supernova feedback results in the relations shown by the blue dashed line. The effect of the supernova feedback is thus illustrated by the difference between the blue dashed and red dotted lines.

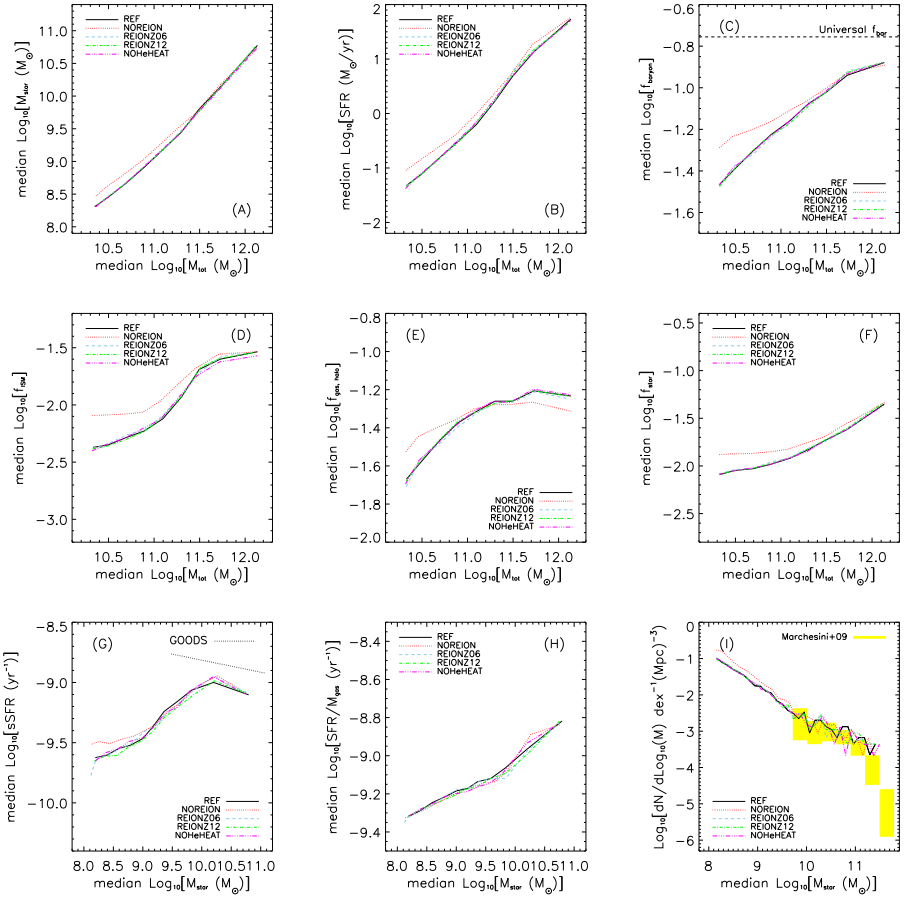

Figure 2.5: Like Fig. 2.2, but now only for a set of simulations in which the reionization implementation is varied. In the reference model (black solid line) the evolving uniform UV background is turned on at $z = 9$. The red dotted line shows a simulation that has no UV background at all, whereas in the blue dashed and the green dot-dashed lines the background is turned on at $z = 6$ and $z = 12$ respectively. The magenta dot-dot-dot-dashed line shows a simulation in which no extra heat input due to helium reionization around $z = 3.5$ is implemented.

2.5 Reionization variations

Fig. 2.5

Reionization is implemented by turning on the model for the UV background from galaxies and quasars of Haardt & Madau (2001). As shown in Wiersma et al. (2009a) the gas is quickly heated to $T \sim 10^4$ K following reionization. Note that we assume the UV background to be uniform and the gas to be optically thin. In our reference model we set the redshift of reionization to $z_r = 9$. To investigate the effects of reionization, we compare to a model without reionization ('*NOREION*') and to two in which we have varied the redshift at which we turn on the UV background: one at redshift 12 ('*REIONZ12*') and one at redshift 6 ('*REIONZ06*'). In '*NOHeHEAT*' we do not inject 2 eV per atom at around $z = 3.5$, as we do in our other models. This energy input is needed to match observationally inferred temperatures in very low density IGM gas. As this is only important for gas that mainly cools through adiabatic expansion, this extra input is not important in galaxies, as we will also show below.

The simple picture of the influence of reionization on the properties of haloes, is that gas residing in haloes with a virial temperature lower than $T_{\rm vir} \sim 10^4$ K will be evaporated. The thermal energy of the gas is in that case higher than the gravitational potential energy of the haloes, so the baryons are not bound to the dark matter. In panel (E) of Fig. 2.5 we compare the gas fractions of haloes in the simulations with the various reionization models. Indeed, in low mass haloes the gas fraction is lower because of reionization. At high masses the gas fraction is slightly lower without reionization than with.

As shown in panel (B) of Fig. 2.5, the effect of reionization is indeed that in low mass haloes the SFR is suppressed (compare the reference model to the model without reionization). The amount of suppression decreases with increasing halo mass. Whether reionization happened at redshift 12, 9 (reference model) or 6, is no longer important at redshift 2.

The extra heat input due to Helium reionization is negligible at gas densities typical of haloes. The unimportance of Helium reionization holds for all properties of the haloes we will investigate in this work. We therefore conclude that the extra heat input to the IGM from helium reionization is only important for the temperature of the IGM and has no effect on the properties of haloes formed in the simulations.

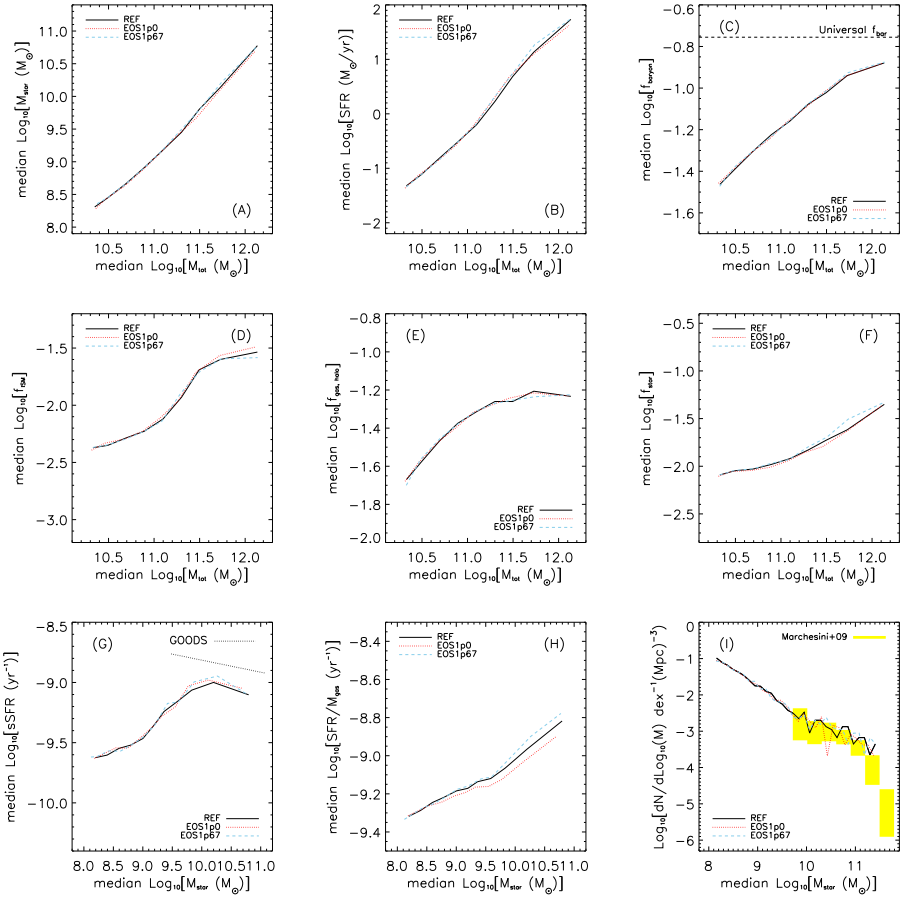

Figure 2.6: Like Fig. 2.2, but now only for a set of simulations in which the equation of state (EoS) for high density gas is varied. In the reference model (black solid line) we use a polytropic EoS with a power law index of $\gamma = 4/3$, because this is numerically convenient. The red dotted line shows the results from a simulation with a shallower (less stiff) EoS, with a power law index of 1 (isothermal). The blue dashed line is the result of a simulation with a stiffer equation of state: $\gamma = 5/3$.

2.6 The polytropic equation of state for high density gas

Fig. 2.6

Our simulations lack both the resolution and the physics to model the multiphase ISM. We therefore impose an effective equation of state (EoS) for all gas particles with densities higher than $n_{\rm H} = 0.1$ cm^{-3}.

As the effectiveness of feedback depends on hydrodynamic effects (mainly drag forces), as we will show later, the equation of state imposed on the high density gas may be important. Although the star formation histories of the isolated disk galaxies of Schaye & Dalla Vecchia (2008) do not strongly depend on the imposed EoS (provided that the star formation law works independently of the equation of state), the structure of the disk (among which the thickness) does.

All imposed EoS are polytropic: $P \propto \rho^{\gamma_{\rm eff}}$. For the reference case, $\gamma_{\rm eff} = 4/3$, both the Jeans mass and the ratio of the Jeans length and the kernel of the SPH particles are independent of the density, making it a numerically convenient choice. Two other EoS are implemented in other runs. The first one is an isothermal equation of state, $\gamma_{\rm eff} = 1$ ('*EOS1p0*'), the other one is adiabatic, $\gamma_{\rm eff} = 5/3$ ('*EOS1p67*').

From the gas density distributions shown in Fig. 2.2.2 it is clear that stiffer equations of state pressurize the gas more strongly, resulting in a smoother distribution of gas. In Paper I it was already shown that the polytropic index had little influence on the total cosmic star formation rate density. In panel (B) of Fig. 2.6 we show that the relation between halo mass and SFR is unaffected by the polytropic index. Although the structure of the galaxies may be significantly altered (see Fig. 2.2.2), their integrated star formation properties are insensitive to the stiffness of the equation of state.

More generally, all physical properties of haloes (except for the gas consumption and star formation time scales) are very insensitive to changes in the polytropic index in the range of 1 – 5/3. This also ensures that more complicated models for the multi-phase ISM will most likely not make haloes behave differently from what is shown in this paper.

2.7 The star formation law

Fig. 2.7

Star formation is implemented using a pressure law. It reproduces the observed star formation rate surface density - gas surface density law, the Kennicutt-Schmidt law (Kennicutt, 1998a): $\dot{\Sigma}_* = A(\Sigma_g/1\ M_\odot\ {\rm pc}^{-2})^n$, with $n = 1.4$ and $A = 1.151 \times 10^{-4}$

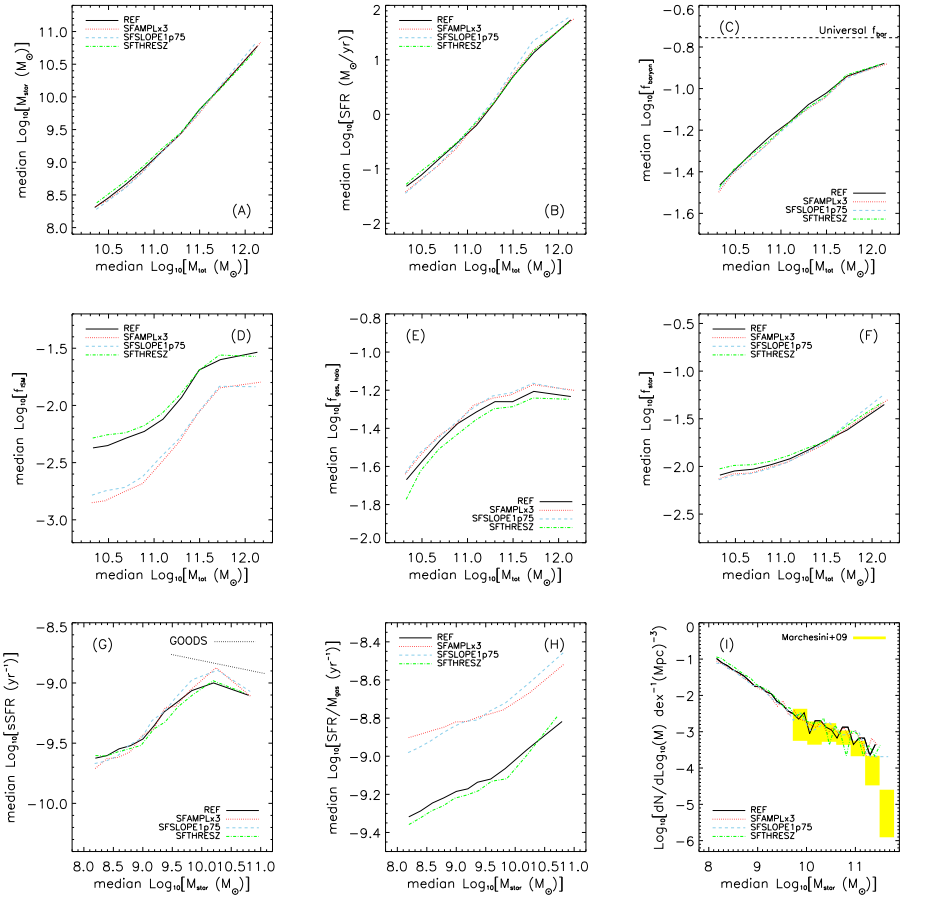

Figure 2.7: Like Fig. 2.2, but now only for a set of simulations in which the in which the only variation is in the implementation of star formation. All simulations reproduce a Kennicutt-Schmidt-like law. The reference model (black solid line) reproduces the KS-law as it is observed, with a slope in the power law relation between gas surface density and star formation rate surface density of 1.4 and the observed normalization. The red dotted line is the result of a simulation which has the same power law slope in the KS law, but has a three times higher amplitude (three times higher star formation rate for given gas density). The model showed with the blue dashed line has steeper dependence of star formation rate on gas density, and at all densities above the star formation threshold, the normalization of the KS-law is higher as well. Both these models therefore have more efficient star formation. The green dot-dashed line shows the results of a simulation in which the star formation threshold is a function of the gas metallicity.

$M_{\odot}\mathrm{yr}^{-1}\ \mathrm{kpc}^{-2}$ (Kennicutt, 1998a), although these values remain controversial (e.g. Blanc et al., 2009). The threshold density for star formation and the normalization of the star formation law are obtained from observations. The normalization should be appropriately scaled to the IMF that is used, see Sect. 2.2.5. For details about our implementation of the star formation law, see Schaye & Dalla Vecchia (2008).

Three different star formation models are run to compare with the standard, observed KS-law. One model uses a factor 3 higher normalization, which implies that for a gas particle with the same pressure, the SFR is a factor 3 higher ('*SFAMPLx3*'). In the other run, the power-law slope of the KS-law is increased from $n = 1.4$ to 1.75 ('*SFSLOPE1p75*'). The normalisation of this model is chosen such that the SFR surface density is the same for $\Sigma_{gas} = 1\ M_{\odot}/\mathrm{kpc}^2$. As this is below the star formation threshold, this KS-law is more efficient than the reference one at all densities. The third variation on the reference model is a model in which the threshold density for star formation (and therefore also for gas going onto the equation of state) depends on the metallicity of the gas, $\rho_{\mathrm{th}} \propto Z^{-0.64}$, such that the threshold density is equal to the reference simulations' if the metallicity is $0.1Z_{\odot}$, ('*SFTHRESHZ*'). This model reproduces the metallicity dependence of the critical surface density for the formation of a cold, molecular phase predicted by Schaye (2004).

As we show in panel (B) of Fig. 2.7 the slope, normalization and threshold density of the Kennicutt-Schmidt law are unimportant for the SFR of a halo. Making star formation at a given density either three times more effective or making the star formation rate a steeper function of the local gas density (and more effective at all densities) does not affect the star formation rate of a halo. Also, making the threshold density for star formation a function of metallicity does not influence the star formation rate of a halo. This indicates strongly that *the global star formation rates of haloes are set by the available fuel and feedback only* and not by the details of how high density gas is treated and how star formation is implemented. In other words: *star formation is self-regulated by the available fuel and feedback*.

If haloes have the same star formation rate, while for a given density gas particles have a higher star formation rate, then the haloes must adapt their reservoir of star forming gas to the higher star formation efficiency. In simulations with more efficient star formation laws, we expect the fraction of gas that is on the EoS to be lower, in order to get the same total SFR and energy injection from feedback into the ISM. In panel (D) of Fig. 2.7 we show that this is indeed the case. While the total gas fractions (not shown) are the same for all implementations of star formation, the amount of gas that is on the EoS, and forming stars, is lower in more efficient star formation models. The more effective star formation laws in these simulations make the gas stay shorter in a star forming phase, as can be seen from panel (H), where we clearly show that the gas consumption time scales are indeed

much shorter, such that the smaller amount of available star forming gas (shown in panel D) forms as many stars in the same halo and releases an equal amount of SN energy back into the ISM. As soon as the density is sufficient the gas is transformed into stars and their feedback prevents other gas from becoming star forming (such that the SFR is unaffected). The feedback accompanied with the more efficient star formation regulates the amount of gas condensing onto the ISM and regulates star formation.

Total baryon fractions and the amount of gas in the halo that is not star forming (panels C and E) are much less sensitive to the efficiency of star formation, as they are largely set by the amount of baryonic accretion and ejective feedback.

2.8 The stellar initial mass function

The stellar initial mass function is under heavy debate in literature. Here, we take the approach of using a popular IMF (Chabrier, 2003) in most simulations. The IMF is important for several aspects of these simulations. First of all, the different ratios of low to high mass stars will result in differences in the integrated colours of stellar populations and in different chemical yields. Also, a different number of SNe per unit stellar mass formed asks for consideration of a change of feedback. In the following two section we will discuss two additional simulations that use different IMFs: Section 2.8.1 shows the simulation results under the assumption of a Salpeter IMF, while Section 2.8.2 discusses a set of simulation with more extreme IMFs in extreme star formation environments.

2.8.1 Salpeter IMF

Fig. 2.8

We also ran a simulation with the Salpeter (1955) IMF, rather than the Chabrier (2003) IMF used in the reference model ('*IMFSALP*'). Due to the absence of a turnover at the low mass end, the fraction of low-mass stars is higher for the Salpeter IMF. Therefore, for every solar mass of stars formed, there is less energy available from high mass stars, as also described in Sect. 2.2.5. We did rescale the normalization of the star formation law accordingly, but we used the same wind parameters as in the reference model (so $1.65 \times 40\% =\sim 66\%$ of the total supernova energy). From Fig. 2.2.2 it can be seen that both IMFs result in galaxy properties that look very similar. Also, in later Sections we will show that the properties of galaxies are not drastically different, although comparisons with observations require rescaling to a consistent IMF to explain differences between models.

In the simulation with the Salpeter IMF ('*IMFSALP*') the fraction of mass in the ISM is lower and the gas consumption time (panels D and H of Fig. 2.8) is

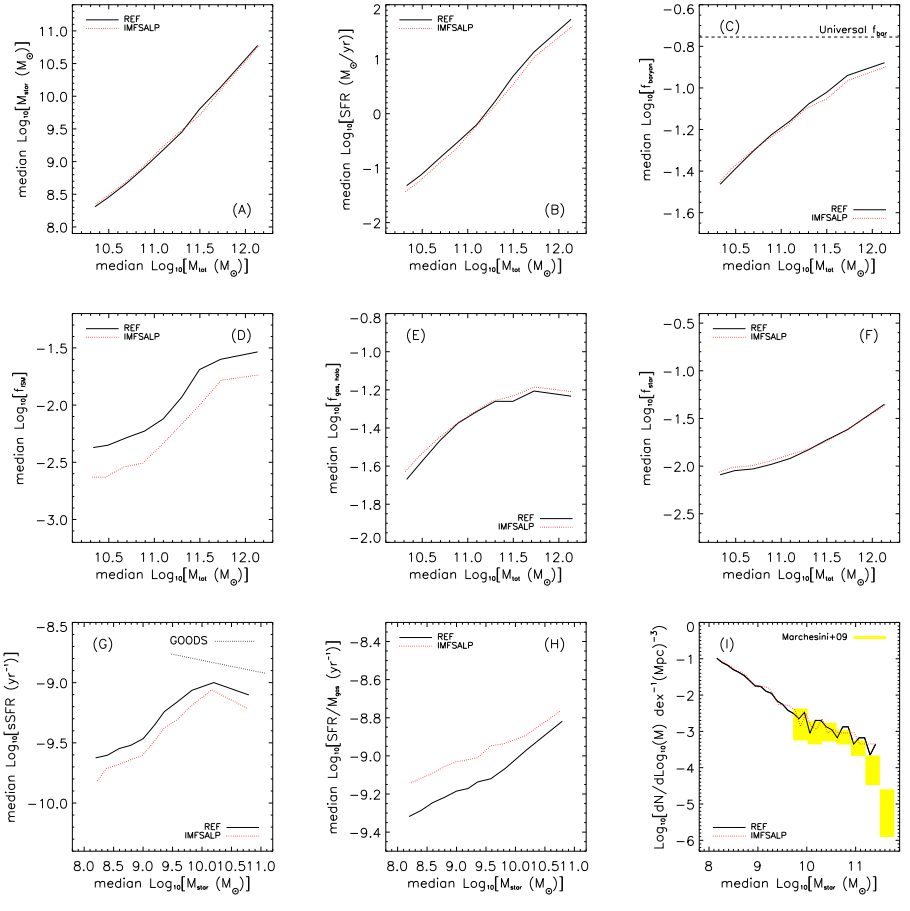

Figure 2.8: Like Fig. 2.2, but now only for two simulations with a different IMF: the reference model (black solid line) uses a Chabrier (2003) IMF, whereas the other simulation (red dotted line) is run assuming a Salpeter (1955) IMF. The main difference between the two is the number of high mass stars formed per unit stellar mass formed, but the high mass slopes are almost identical.

slightly shorter than in the reference model. This is due to the lower amount of gas turned back into the ISM, due to the lower fraction of massive stars per unit stellar mass. The regulation of star formation by SN feedback and the fact that the total energy in the winds are the same for both simulations result in a less massive star forming gas reservoir in the ISM of the galaxies, and very similar stellar content of the haloes (panels A and F).

In panel (H) of Figs. 2.6, 2.7 and 2.8, where the simulations with different EoS indices, KS-laws and stellar IMFs are shown we see the self-regulation of the star formation illustrated once more. The polytropic EoS index is unimportant for the gas consumption time scale. Making the Kennicutt-Schmidt law more effective, though, results in much shorter gas consumption time scales. This is reasonable, as the same gas density/pressure results in a higher star formation rate in both these models, and is explained already in Sect. 2.7. Below, when we discuss different SN feedback implementations we will see that the SN feedback is crucial in setting the star formation properties of haloes. The cooling of gas and the feedback of energy into the ISM work together such as to put back the same amount of SN energy into the ISM (for a given feedback model), regardless of the details of the high density gas or the star formation law.

2.8.2 Simulations with a top-heavy IMF at high pressures

Fig. 2.9

In order to keep SN feedback effective in high mass galaxies, higher wind velocities are needed (as will be shown below). In another set of simulations (‘*DBLIMF*’) stars are assumed to form with a top-heavy IMF (an IMF with power law $\mathrm{d}N/\mathrm{d}M \propto M^{-1}$) if the gas pressure exceeds $P/k = 2.0 \times 10^6$ cm^{-3} K (evaluated at the resolution limit of the simulations). Observationally, there is some evidence that star formation in gas with high pressure (such as starbursts and in the centre of the Galaxy) occurs with an IMF that is flatter than Chabrier (e.g. McCrady et al., 2003; Stolte et al., 2005; Maness et al., 2007).

The total energy from Supernovae Type II per unit stellar mass formed is higher for a top-heavy IMF (a factor of 7, comparing the aforementioned top-heavy IMF with the default Chabrier IMF). This extra energy can be used to increase either the wind mass loading or the wind velocity. We tried both options. To facilitate comparisons with the reference run, in one run the velocity was kept fixed at 600 km s^{-1}, but the mass loading was set to $\eta = 14$ (‘*ML14*’). In the other one, the mass loading was kept fixed at $\eta = 2$ and the wind velocity was increased to $v_w = 1618$ km s^{-1} (‘*V1618*’).

When changing the IMF suddenly at some pressure, it is not immediately clear what to do with the star formation law. The Kennicutt-Schmidt law is inferred

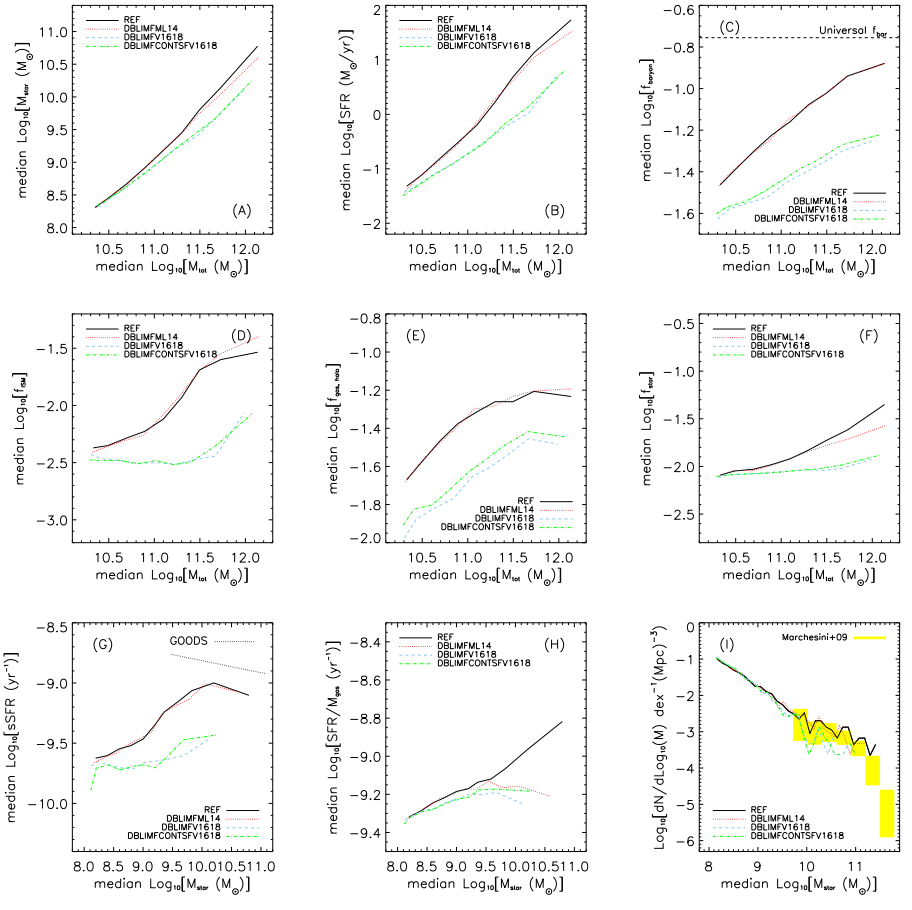

Figure 2.9: Like Fig. 2.2, but now only for a set of simulations in which a top-heavy IMF is used for star formation at high pressure. The reference model (without top-heavy IMF) is shown by the black solid line. The extra available SN energy per unit stelar mass formed can be put in mass loading or velocity of the winds, which is the difference between the red dotted line (mass loading 7 times higher than in the reference model, at the same wind velocity) and the blue dashed line (mass loading as in the reference model, but a wind velocity of 1618 km s^{-1}). With a jump in the IMF at some pressure, one can either let the star formation rate be a continuous function of the density, or let the rate of formation of massive stars (which is what is observed) be continuous with density. This is the difference between the blue dashed (continuous formation of massive stars) line and the green dot-dashed line (continuous star formation rate, so a jump in the formation rate of massive stars at some pressure).

from observations probing massive stars. Therefore, the total SFR depends on how many low-mass stars are formed together with these massive stars. When changing the IMF, the star formation law can be changed in two ways:

1. From observations there is no indication of a discontinuity in the formation rate of massive stars with pressure. Although this is most likely the result of the IMF being a continuous function of SFR or pressure (if there is a relation at all), we nevertheless implemented a model that changes the normalization of the KS-law such that the formation of massive stars is continuous, resulting in a discontinuous SFR as a function of pressure (the KS-law normalization drops at the pressure above which the IMF is top-heavy). These models are indicated by '*DBLIMF*'.

2. If the (total) SFR as a function of pressure is continuous, the formation of massive stars must be discontinuous, given that we assumed the IMF to change suddenly above some critical pressure. Models with a continuous SFR include '*DBLIMFCONTSF*' in their 'name'.

In Sect. 2.7 we showed that the normalization of the KS-law does not influence the mass function or SFR distributions of galaxies. We therefore expect differences with respect to the reference model to be due to the extra energy input from SN feedback and/or the increased rate of production of metals that results from a top-heavy IMF.

When comparing simulations to observations, we do not correct for the stellar mass of simulations with a double IMF. On average, only $\sim$ 10% of the star particles in the simulation box formed with a top-heavy IMF (this depends slightly on resolution and hardly on whether the rate of formation of massive stars, or rather of all stars together is a continuous function of density). In Schaye et al. (2010) it was shown that at late times, this correction should be made, but at $z = 2$ the integrated SFR of the universe is not different whether or not the SFRs of particles at pressures higher than the threshold pressure for the top-heavy IMF are corrected for another assumed IMF (the SFR inferred under a Chabrier IMF would be higher than the actual SFR).

The extra energy due to the higher fraction of high mass stars, only has an effect when these particles are launched at sufficiently high velocities. Therefore, the simulation that uses the extra energy to increase the mass loading do not show any change with respect to the reference model for massive galaxies, as the winds do not escape the galaxies. If the extra energy is used to increase the wind velocity, then the feedback does become more effective. The extra energy input is more important in high mass haloes, as the fraction of stars formed at a density above the double IMF threshold increases with halo mass (in total $\sim$10% of the stars in

the simulation are formed with a top heavy IMF, at this resolution). Whether we choose to have a total SFR that is continuous with pressure or a continuous rate of formation of massive stars (and therefore a jump in total SFR as a function of pressure) is not important.

The baryon fraction in the '*DBLIMFML14*' is indistinguishable from the reference model (note that the stellar mass fractions are slightly lower in the simulation with a double IMF and the excess energy put in mass loading), indicating that the gas with the extra energy from the excess of high mass stars does perturb the galaxy more and keep the ISM at low pressure, but the baryons do not escape the halo. They do escape the halo in the double IMF simulations with the extra energy put in wind velocity, as shown in panel (C) of Fig. 2.9. From panel (B) of Fig. 2.9 it is clear that putting the extra available energy from supernovae in top-heavy IMF stellar populations in mass loading did not change the SFR of a galaxy. In panel (H) it can be seen that the gas consumption time scale, nevertheless, has increased by the same amount as it did for the double IMF simulations that put the energy in wind velocity. So although, as a function of stellar mass the star formation rates of the reference model and '*DBLIMFML14*' are similar, the gas consumption times are shorter in the reference model. We note that, as shown in panel (F), the stellar mass fraction of this simulation is lower than that of the reference model, and we can see in panel (D) that in this simulation the star forming gas mass fraction as a function of halo mass is *higher* than in the reference model. We can conclude that this form of feedback, which has $\sim$7 times more energy, results in a *larger* reservoir of star forming gas, which is used up more slowly, as it is kept kept at lower pressure. The high mass loading in the simulation 'puffs up' the galaxy, such that although there is a large reservoir of gas to form stars from, the SFR still is the same as it would be without a fraction of the stars formed with a top heavy IMF.

A tiny difference in the stellar mass fraction in the simulation with a top-heavy IMF for high pressure star formation that puts the excess energy of SNe in mass loading: the extra available energy results in a minor decrease in stellar mass fraction by $z = 2$, whereas the difference in (s)SFR is hardly visible. Only a small fraction of the star particles forms with a top-heavy IMF, but those star particles loose mass quickly. Besides, the stellar mass content is the integral of the SFR over time, so tiny differences in the SFR add up to a noticeable difference in stellar mass.

2.9 Supernova feedback

In order to run simulations without any feedback form supernovae (SNe) all the way to the final redshift, we turned off metal-line cooling. The very high metallic-

ities and, consequently, very high densities reached would otherwise result in very high cooling rates and very short time steps. Therefore, in order to compare simulations with and without SN feedback, we compare the simulation without metal-line cooling and SN feedback ('*NOSN_NOZCOOL'*) with the simulation without metal-line cooling ('*NOZCOOL'*) in Fig. 2.4.

Star formation in haloes will in general be regulated by the amount of available fuel, and therefore the inflow rate of cold gas and by the feedback that accompanies the formation of massive stars, which may prevent or suppress further star formation by removing or heating the available gas. In panel (B) of Fig. 2.4 we compare the SFR as a function of halo mass for simulations without SN feedback (and without metal-line cooling) with the reference model, which does include both SN feedback and metal-line cooling. SN feedback accounts for the difference between the '*NOSN_NOZCOOL*' and '*NOZCOOL*' simulations, shown by the blue dashed and red dotted curves, respectively. The SFR in the simulation without SN feedback is much higher at a given halo mass. The difference declines with increasing halo mass, as the effect of SN feedback becomes less important for more massive systems (e.g. White & Frenk, 1991).

In Fig. 2.9.1 we compare the stellar mass fractions of the two simulations of Fig. 2.3 with the same cosmology, but a factor two difference in wind energy (the energy difference is put in mass loading), but now in a 100 Mpc/h box (using $2x512^3$ particles as well) at redshift zero. It can be clearly seen that at some mass the winds become very ineffective and the stellar mass fractions of the halo rise steeply ($10^{\sim 11.2} M_\odot$ at redshift 2 and $10^{\sim 12.2} M_\odot$ at redshift zero and at 8 times lower resolution). Below this mass, in the regime of effective winds, the difference in stellar mass fraction is exactly the factor two difference in feedback energy. Although it is mainly velocity that sets the effectiveness of the winds, at a given velocity the stellar mass fraction is still a factor two lower for a simulation with a mass loading of the wind that is a factor 2 lower. This shows how well self-regulation of the star formation by supernova feedback works.

2.9.1 Winds with constant energy per unit stellar mass formed

Fig. 2.10

In the set of models shown in Fig. 2.10 we vary the parameters of the winds resulting from massive stars and core collapse supernovae. More specifically, we compare 4 simulations which all use the same feedback energy per unit stellar mass formed. The winds are implemented kinetically and are specified by the mass loading (the amount of mass put in the wind per unit of mass transformed into stars) η (denoted by '*ML*' in the simulation names) and the velocity with which this mass is kicked, v_w. For more detailed information about the wind implementation, see

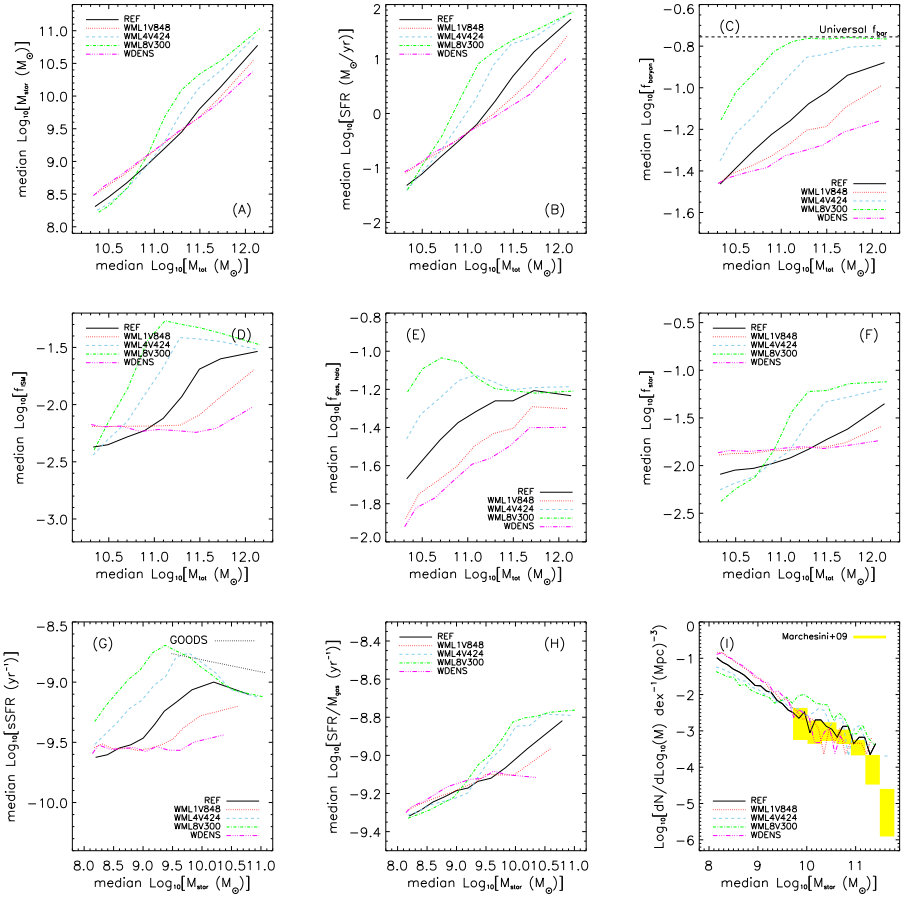

Figure 2.10: Like Fig. 2.2, but now only for a set of simulations in which the wind velocity and mass loading are varied. The reference simulation (black solid line) has a mass loading of $\eta = 2$ and a wind velocity of 600 km s^{-1}. The simulations shown by the red dotted, blue dashed and green dot-dashed lines show variations on this at the same energy, but with the mass loading changing by a factor of 2 (and, therefore, the velocity by a factor $\sqrt{2}$), giving a mass loading of 1 (a velocity of 848 km s^{-1}, red dotted line), 4 (a velocity of 424 km s^{-1}, blue dashed line) and 8 (velocity of 300 km s^{-1}, green dot-dashed line). The magenta dot-dot-dot-dashed line represents a simulation which has a mass loading and velocity dependent on the local density, such that the energy in the wind is still the same and the velocity is proportional to the local sound speed.

Dalla Vecchia & Schaye (2008). The reference simulation assumes a mass loading of 2, and a wind velocity of 600 km s^{-1}, which corresponds to 40 per cent of the energy available from core collapse SNe. The wind kinetic energy scales linearly with mass and quadratically with velocity, a change of factor n in the mass loading requires a factor $n^{-1/2}$ change in the wind velocity. The mass loadings in the four simulations are 1, 2 (reference), 4 and 8, with corresponding velocities of 848, 600, 424 and 300 km/s, respectively. An example of the notation used throughout the paper would be '*WML1V848*' for $\eta = 1$ and $v_w = 848$ km s^{-1}.

We expect that winds with a constant velocity will not be efficient in every halo. Aside from gravity, which sets a gravitational escape velocity, ambient gas has to be swept up and dragged along. This will slow down the wind due to the conservation of momentum and due to ram pressure forces. This gas drag increases with the pressure of the ISM and thus with the mass of the galaxy. Above some halo mass, the winds will be slowed down too much and will not escape the galaxy any longer. Dalla Vecchia & Schaye (2008) showed explicitly that slowing down the winds and making them inefficient above some mass is caused by gas drag rather than gravity (we will show this again below, in Sect. 2.9.2). Because of the dependence of the mass at which the winds become ineffective (as shown below) we have also performed simulations in which the wind velocity scales with local properties. One such simulation, with constant energy in the winds, is called '*WDENS*'. In this simulation the distribution of the energy over mass and velocity is determined by the local gas density (i.e. the density of the gas from which the star particle formed) as follows: $v_w \propto \rho^{1/6}$, $\eta \propto \rho^{-1/3}$, which implies $v_w \propto c_s$ for the effective equation of state $P \propto \rho^{4/3}$ that we impose onto the ISM (see Section 2.6), where c_s is the sound speed. The normalization is such that the wind velocity and mass loading are the same as in the reference model if the gas density equals the star formation threshold, i.e. $n_{\rm H} = 0.1$ cm^{-3}. From Fig. 2.2.2 it is clear that this variation in wind velocities does not result in very different appearances for the galaxies, whereas the star formation properties differ strongly.

In Fig. 2.10, the simulations with constant wind energies, but different mass loading factors and wind velocities are compared. At low halo mass, the models are very comparable. At some halo mass the SFR (panel B) suddenly goes up strongly, and the mass at which this happens increases with wind velocity. Comparing the different models in Fig. 2.10 to the '*NOSN_NOZCOOL*' in Fig. 2.4 shows that the relation between SFR and halo mass is, at high stellar masses, similar to the simulation without any feedback (and without metal line cooling), suggesting that the feedback indeed is completely ineffective. High wind velocities are slightly less efficient at low halo mass, because of the lower mass loading in the winds. For the low mass systems, the wind velocity is not important, as the winds escape the halo anyway.

For the '*WDENS*' model, the energy injected in the wind per unit stellar mass is also the same as in the reference model, but the initial wind velocity scales with the local sound speed. The relation between halo mass and SFR is even shallower than it is for the run with $v_w = 848$ km s^{-1}, indicating that the feedback is efficient for all haloes. At high masses, this is the most effective wind model with constant energy.

We have seen that for haloes that have ineffective feedback (due to too low velocities), the star formation rate is very high, and the relation between star formation rate and mass has a shallower slope than for simulations with effective SN feedback. One important result that can be seen from the comparison of the reference model with the model without metal-line cooling (Fig. 2.4) is that turning off metal-line cooling reduces the star formation mostly in the highest mass haloes. Although this model has the feedback as in the reference model, the star formation rate apparently is lower. In paper I it was already argued that metals reduce the efficiency of the winds. The low wind velocities will result in more centrally concentrated metal distributions, reducing the efficiency of the winds more strongly in high mass, than in low mass haloes. Comparing the simulations in Fig. 2.10 with the simulation without metal-line cooling in Fig. 2.4 shows that the transition from effective winds to ineffective winds is much more gradual in the absence of metal-line cooling.

As is clear from panel (I) of Fig. 2.10, bringing down the slope of the low mass end of the stellar mass function can be attained by increasing the mass loading factor in constant energy winds. The highest mass loading still gives a low mass end slope that is steeper than power law fits to the low mass end in the observations, although the discrepancy only occurs on masses lower than those observed.

In panel (F) of Fig. 2.10 we show the stellar mass fractions of the simulations of different wind models with the same energy and it can be seen that at the very low mass end, the simulations with a low velocity (and therefore high mass loadings) the stellar mass fractions are lower than for simulations with a lower mass loading. This also reflects in a shallower low mass end slope of the stellar mass function, as illustrated in panel (I). Fig. 2.9.1 shows the stellar mass fractions of two simulations which differ by a factor of 2 in feedback energy (as described in Section 2.3). The difference in energy is used to increase the mass loading at fixed velocity, such that the inefficiency of the winds kicks in at the same halo mass. At the low halo mass end, the difference in stellar mass fractions of the two simulations is a factor of 2. This illustrates how the energy in the feedback directly sets the fraction of the mass that transforms into stars.

The baryon fractions and the fraction of the mass in warm-hot gas in the halo (panels C and E) show that at low halo masses, the amount of gas (or, equivalently, baryons) in the halo is higher for lower wind velocities. These winds, even if they

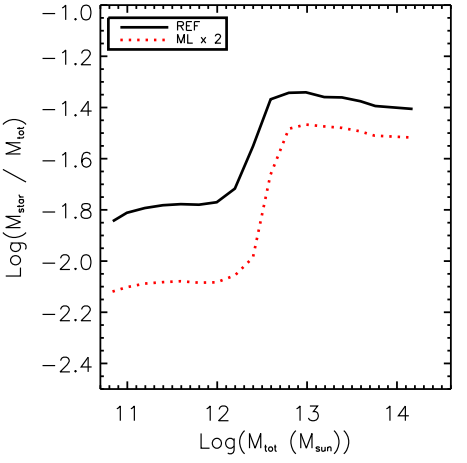

Figure 2.11: The stellar mass fraction as a function of halo mass in 100 h^{-1}Mpc boxes with 512^3 particles at redshift 0. We compare here two models with each other that differ in supernova feedback energy by a factor of two (two times higher mass loading in the wind, same wind velocity) at redshift 0.

do escape the ISM and near vicinity of the galaxy, can not escape their parent halo.

A comparison of (G) and (H) is once again an illustration of the regulation of star formation by SNe. The gas consumption time scales (in the regime where the winds are all efficient) are very similar. Per unit stellar mass formed, the same amount of SN energy is fed back into the ISM and used efficiently to suppress star formation. The sSFR, as displayed in panel (G) are different, because the build-up of stellar mass has been different. The gas consumption time scale is likely the best indicator for at which mass the winds become inefficient.

2.9.2 Hydrodynamically decoupled winds

Fig. 2.12

Most simulations using the code GADGET-2 employ the Springel & Hernquist (2003a) implementation of kinetic SN feedback. In this model the wind particles, once launched, are temporarily decoupled from the hydrodynamics. The coupling is turned on again after a fixed amount of time (50 Myr), or when the density of the wind particle falls below some value (10% of the star formation density threshold, i.e. when $n_{\rm H} < 10^{-2}$ cm^{-3}), whichever occurs first. During decoupling a gas particle experiences gravity, but no hydrodynamic drag. Decoupling the winds is expected to result in a different SFR for high mass galaxies, as feedback will

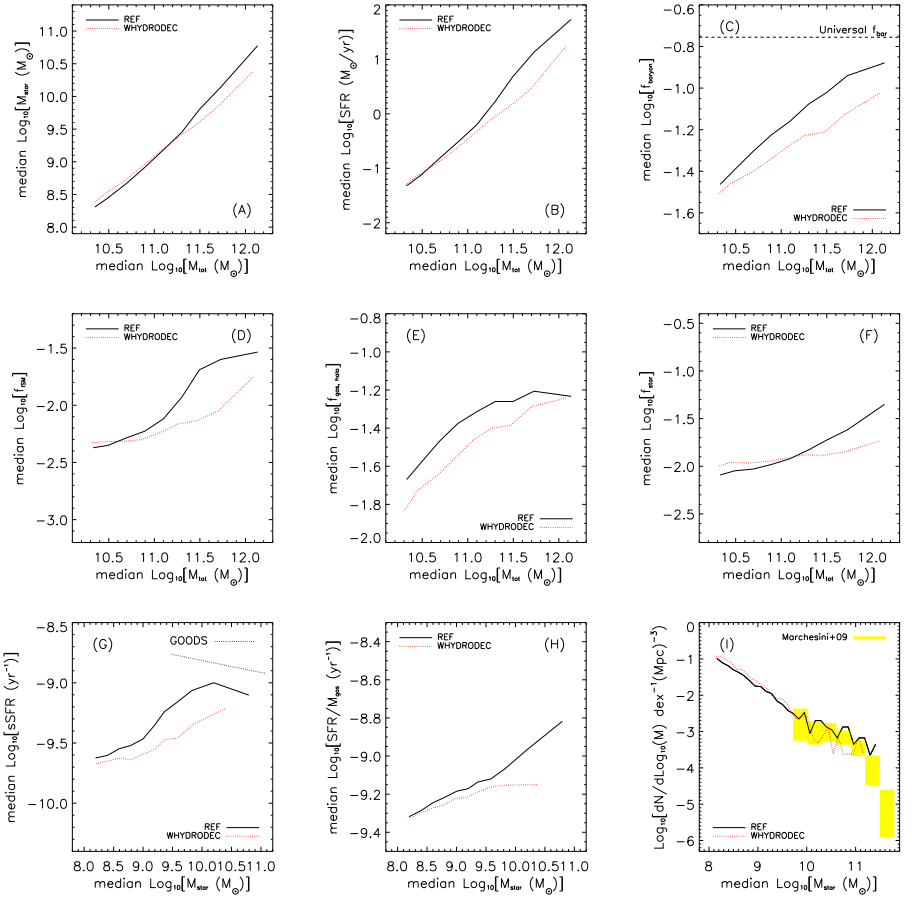

Figure 2.12: Like Fig. 2.2, but comparing only the reference simulation (black solid line) and the simulation in which the wind particles are temporarily decoupled from the hydrodynamics (red dotted line).

remain efficient in the halo mass range where our reference model becomes inefficient due to gas drag in the ISM (see Dalla Vecchia & Schaye, 2008). In practice, decoupling the wind particles means that the wind particles fly out of the galaxy before they couple again, and therefore do not drag any other ISM particles. The winds leave the galaxies at much higher velocities than in the *OWLS* reference model (and all other wind models as well), mimicking simulations that use a much higher wind energy and velocity. For a detailed study of the effect of decoupling for the case of isolated disk galaxy simulations, see Dalla Vecchia & Schaye (2008). For comparison, we have also run a model with the Springel & Hernquist (2003a) decoupling, denoted '*WHYDRODEC*'. Note that isolated galaxies formed with decoupled winds look less realistic, particularly at low masses (Dalla Vecchia & Schaye, 2008). From Fig. 2.2.2 we can see that the gas density outside the disc is much higher in this model.

Decoupling the wind hydrodynamically gives effective feedback for all haloes, as the mass of the gas that has to be dragged along is zero, so all particles launched in the wind escape the galaxy. Therefore, the SFR for this simulation is lower at (relatively) high masses than the reference model. For the lowest mass, where the reference model also has very effective feedback, as discussed in Sect. 2.9.1, the difference decreases, as shown in Fig. 2.12. From this large difference between the '*WHYDRODEC*' and the '*REF*' models we can conclude that it is not gravity (which acts on the winds in both simulations), but the hydrodynamic forces which makes the winds less prone to escape in high mass haloes, as was already shown by Dalla Vecchia & Schaye (2008).

Because of the lag of hydrodynamic coupling in the first few tens of Myrs, the gas flows out to large distances. When it couples to the hydrodynamics again, it still has a larger velocity than it would have had at the same location, if the coupling was never broken. Therefore, also at larger distances it is still easier for the gas to flow out. This results in the lower baryon fractions, and fractions of mass in gas in the halo in the model with hydrodynamic decoupling, as is shown in panels (C) and (E) of Fig. 2.12. The fact that the gas does not drag along surrounding gas while it is in the ISM of the galaxy it is launched from results in a larger fraction of the mass in the ISM in the lowest mass haloes (with decoupling, more mass would have been dragged outwards), as shown in panel (D). This also results in a slightly higher stellar mass fraction at low mass, as shown in panel (F).

2.9.3 Thermal SN feedback

Fig. 2.13

Instead of launching the wind by injecting kinetic energy, we also use an implementation of thermal feedback, in which we inject thermal energy into the gas

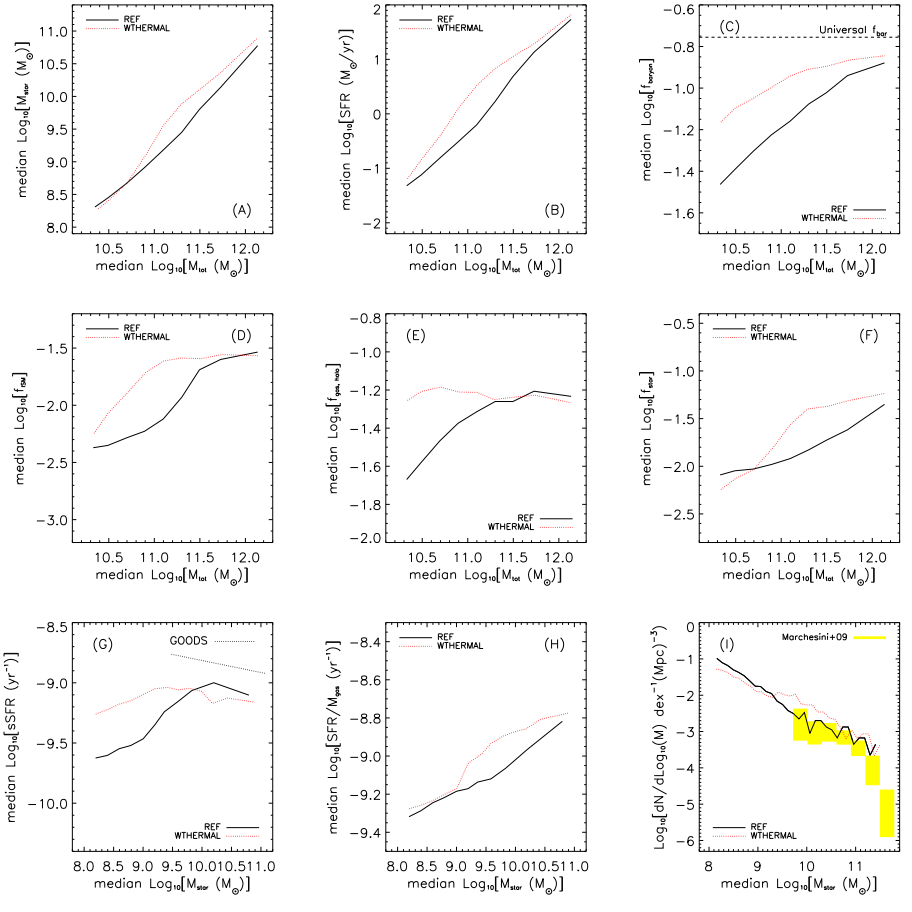

Figure 2.13: Like Fig. 2.2, but comparing only the reference simulation (black solid line) and the simulation in which the supernova feedback is implemented thermally, instead of kinetically (red dotted line).

surrounding the star particle that has exploding SN. If the available energy is distributed amongst all SPH neighbours, the rise in temperature corresponding to the energy input is so low that radiative cooling will be very efficient. In that case, particles will immediately radiate away this energy and feedback will have little effect, unless the cooling is temporarily turned off (Mori et al., 1997; Thacker & Couchman, 2000; Kay et al., 2002; Sommer-Larsen et al., 2003; Brook et al., 2004; Stinson et al., 2006). Therefore, we choose to inject the thermal energy into neighbouring gas particles, ensuring that the temperature of the particle rises to within the radiatively inefficient regime, using a temperature rise of $\Delta T^* = 10^{7.5}$ K. The expectation value for the number of particles to heat is then 1 for 40% of the available SN energy. For details on the thermal feedback implementation we refer to Dalla Vecchia & Schaye (in prep.).

Although injecting 100% of the available SN energy can be justified in the case of thermal feedback (the 40% chosen in the other implementations described above allowed for radiative losses), we choose to use 40% in order to facilitate comparison with the other models.

The thermal implementation of SN feedback is shown in Fig. 2.13. Although the same energy is used per unit stellar mass formed, the thermal implementation is less effective than the kinetic implementation. Note that it is still much more effective than thermal implementations used in literature (e.g. Kay et al., 2003) and that we still use only 40% of the available SN energy, whereas 100% could be justified in these models as well. At low masses, the SFRs are higher than the reference model, and get close to the wind models with low velocities (v_w = 424 km s^{-1}). For higher masses, the relation between halo mass and SFR joins the tracks of ineffective feedback for the simulations discussed in the previous section.

The thermal implementation also is more effective at low masses than at high masses, as illustrated by the gas consumption time scale (panel H), the stellar mass fraction (panel F) and the fraction of the mass in the ISM (panel D). Whenever thermal energy is transferred to gas particles, these particles respond by adiabatic expansion due to their suddenly higher temperature. While expanding, they push away other gas particles, and as such a large scale outflow may still arise. Depending on the mass of a galaxy, the cooling time (due to different metallicities and different pressures) and the surrounding ambient pressure (which makes it harder to expand) influence the effectiveness of this form of feedback.

2.9.4 'Momentum-driven' wind models

Fig. 2.14

Galactic winds could be driven by radiation pressure on dust grains in the wind, which drag along the gas (Murray et al., 2005). Here the driving force of the wind

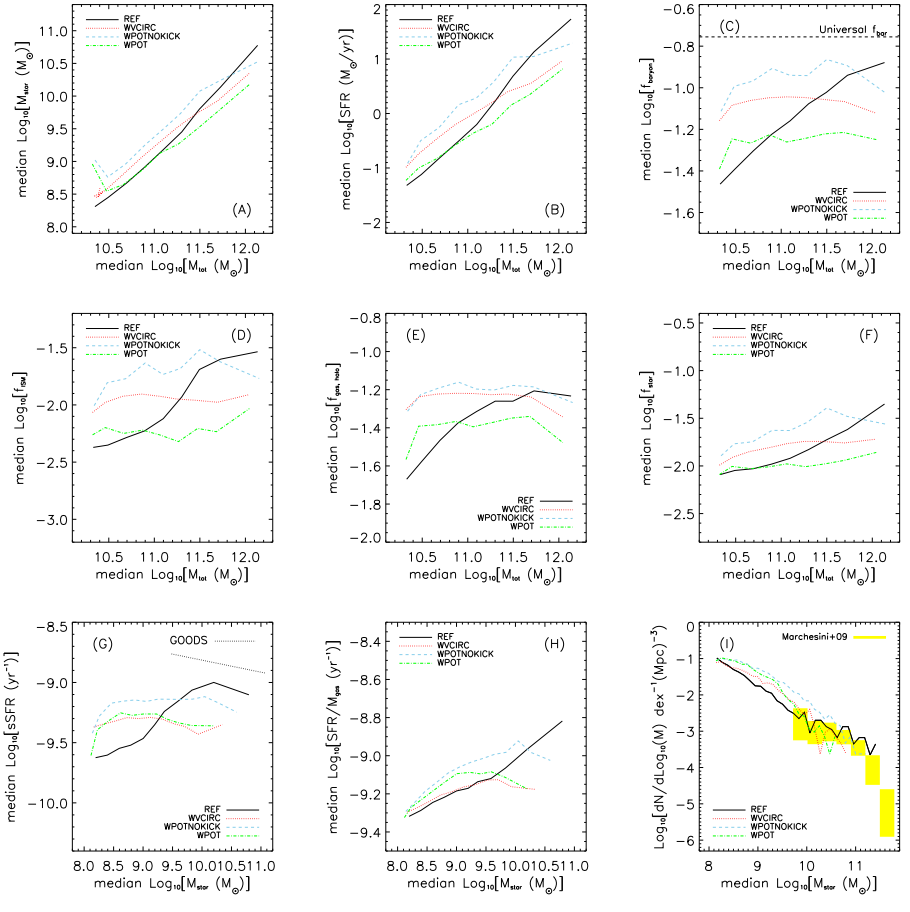

Figure 2.14: Like Fig. 2.2, but comparing a set of simulations with momentum driven winds to the reference simulation (black solid line). In *'WVCIRC'* (red dotted line), the wind velocity depends on the circular velocity of the halo the wind is launched from, while in *'WPOTNOKICK'* and *'WPOT'* it is the local gravitational potential that sets the wind velocity (without and with a kick, shown by the blue dashed and green dot-dashed lines respectively). The energy in these winds is not constant and generally exceeds the energy in the reference simulation.

is the radiation pressure which injects momentum into the outflow and therefore such models live under the common name of 'momentum driven winds'. As it is the stellar continuum radiation driving the dust grains, the efficiency of such winds increases with galaxy luminosity and, therefore, mass.

We implemented some such models, which are similar to the momentum driven wind models used by Oppenheimer & Davé (2006, 2008). Here, the energy of the wind is not constant, but depends on either the local potential ('*WPOTNOKICK*') or the circular velocity, $v_c = \sqrt{GM_{vir}/R_{vir}}$ of the halo the wind is launched from ('*WVCIRC*'). Note that the energy put in the wind per unit stellar mass formed scales with the mass ($E \propto M^{1/3}$) and exceeds the available energy from SNe for the most massive galaxies ($M \gtrsim 10^{12.5}\ M_{\odot}$, the exact mass of equality is redshift dependent, due to the redshift dependence of the virial radius). We show in Appendix 2.11 that, compared to the momentum available from radiation pressure, the momentum in the winds in these simulations is overestimated by an order of magnitude or more.

In '*WVCIRC*' the wind velocity and mass loading are given by $v_w = (3 + n)v_c/\sqrt{2}$ and $\eta = \frac{1}{\sqrt{2}} \times (v_c/v_{\rm crit})^{-1}$, where n and $v_{\rm crit}$ are parameters, set to 2 and 150 km s^{-1}, respectively. From the image in Fig. 2.2.2 it can be seen that the '*WVCIRC*' wind model completely disrupts the disc of the galaxy.

In the '*WPOTNOKICK*' model, the wind velocity is given by $v_w = 3\sigma$, where σ is the velocity dispersion, calculated from the gravitational potential: $\sigma = \sqrt{-\Phi/2}$. In '*WPOT*' we added an extra kick in the velocity of $2 \times \sigma$, as did Oppenheimer & Davé (2006). These models both have velocities that depend on the local gravitational potential. This potential is, however, more closely related to the large-scale structure you are in, than to the mass of the halo. Note that in all models we do couple the wind particles to the hydrodynamics, whereas earlier studies did not.

The effects of the different momentum driven wind models are shown in Fig. 2.14. Scaling the energy with the potential of the star forming particle or with the mass of the halo the wind is launched from results in relatively shallow relations between SFR and halo mass. The relation for '*WPOTNOKICK*' is noisier than the other momentum driven wind models, because the local potential tells you more about the large scale structure the halo is in than about the actual mass of the halo, and therefore the energies at given halo mass scatter more. Giving the wind an extra kick in velocity on top of the kick it would be given in '*WPOTNOKICK*', as done in '*WPOT*', results in even stronger feedback and correspondingly lower SFRs.

For most simulations, there is a very tight correlation between the gas consumption time scale and stellar mass, with not much scatter between the simulations, especially at the low stellar mass end. As long as the feedback is efficient, the

gas consumption time scale is a decreasing function of stellar mass, independent of wind velocity and mass loading. The energy in the winds make some difference as can be seen in panel (H) of Fig. 2.14, where the momentum driven wind models are plotted.

In panel (C) of Fig. 2.14 one can read off the effectiveness of the momentum driven wind models in terms of the baryon fractions of the haloes. These models are successfully used by Oppenheimer & Davé (2006); Davé & Oppenheimer (2007); Finlator et al. (2007); Oppenheimer & Davé (2008) to fit the $z = 6$ luminosity function, the evolution of C IV and to explain the galaxy mass-metallicity relation and $z = 0$ IGM abundances. Here we show that the haloes have roughly constant baryon fractions with halo mass and fairly high compared to most other models, except in the most massive haloes, where the other models overshoot the momentum driven wind models. Tests on the enrichment of the IGM in our simulations are studied in more detail in future studies.

In panel (F) of Fig. 2.4 we show the stellar mass fraction as a function of total halo mass for the simulations described in Sect. 2.9. More efficient feedback (so, high wind velocities in high mass haloes, like in the momentum-driven wind models, the hydrodynamically decoupled winds and the simulations with a double IMF where the excess energy is put in wind velocity) results in flatter stellar mass fractions as a function of mass. For haloes for which the wind velocity is too low for the winds to escape, the stellar mass fraction shoots up. Only for the very most massive haloes, for which some of the SN feedback models in Fig. 2.10 (the constant wind velocity models) are very inefficient, some simulations have a stellar mass fraction approaching the stellar mass fraction of the simulation without SN feedback and without cooling. If the wind velocity is sufficiently high to make the feedback efficient, the mass loading will set the amount of fuel for star formation that is removed from the system. In the momentum driven wind models as discussed here, the mass loading becomes higher for lower mass galaxies, thats why the slope of the stellar mass function (panel I) is getting shallower towards lower masses.

2.10 AGN feedback

Fig. 2.15

Many varieties of AGN feedback have been implemented, see Booth & Schaye (2009), of which we will show only one. Haloes are identified at small time intervals during simulation runtime, with FoF, as described earlier. If a halo has a mass of at least $4 \times 10^{10}\ M_{\odot}$ and no black hole yet, a seed black hole is placed at the position of the most bound baryonic particle. The mass of the seed black hole is

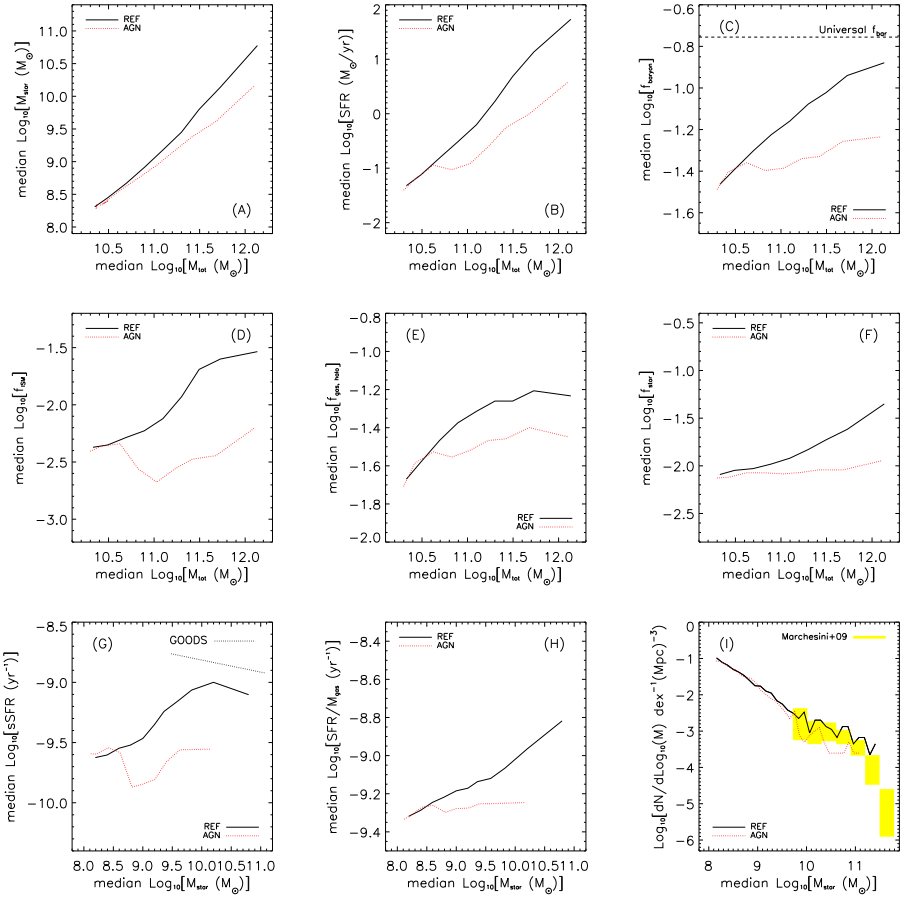

Figure 2.15: Like Fig. 2.2, but only comparing the reference model (black solid line) to a simulation that includes AGN feedback (red dotted line).

15.6 times smaller than the mass of a baryonic particle (9×10^4 $M_\odot$). The black hole is then grown by accretion, limited by the Eddington limit, or mergers. This growth is self-regulated, in the sense that the black holes grow very fast (at the Eddington rate) onto the black hole mass - stellar mass relation and then continues to grow along the observed relations. AGN feedback on the surrounding gas is implemented thermally, i.e. the black hole stores its accreted energy until the feedback will heat one neighbour (stochastically) by 10^8 K. The radiative efficiency is assumed to be 10% and 15% of the feedback energy is assumed to couple to the ISM, i.e. the feedback energy $\dot{E}_{feed} = 0.015\dot{m}_{accr}c^2$.

As described by Booth & Schaye (2009), this model reproduces the observed black hole scaling relations, the black hole fundamental plane and the global black hole density of the Universe. Fig. 2.2.2 shows that AGN feedback is the only model as destructive as the momentum driven winds in terms of removing gas from the haloes. This is also visible in panels (C - E) of Fig. 2.15, where it is obvious that the ISM and halo gas content (and thus the baryonic content, which is dominated by gas in the halo) of galaxies is strongly reduced above some halo mass.

AGN feedback has been argued to suppress star formation in high mass haloes (e.g. Di Matteo et al., 2005; Croton et al., 2006; Bower et al., 2008; Booth & Schaye, 2009; McCarthy & Others, 2009). In order to overcome cooling catastrophes in high mass haloes, a continuous source of heating is necessary, shutting off almost all star formation (e.g. Edge & Stewart, 1991; Markevitch, 1998; Khalatyan et al., 2008). In panel (B) of Fig. 2.15 we show the halo SFR as a function of mass for the AGN feedback model. Indeed, the effect of AGN is strongest at high masses, but is already noticeable for masses as low as $10^{\sim 10.6}$ $M_\odot$. When seed black holes are inserted into haloes, the AGN quickly grow onto the scaling relations, as shown by Booth & Schaye (2009) and are effective in heating up the gas in the central regions of the galaxy and decreasing the SFR. Panels (B) and (F) of Fig. 2.15 shows that the inclusion of AGN feedback indeed lowers the star formation rate of haloes and, as a result, the stellar mass fractions.

From the panels (D), (E) and (F) it can be seen that AGN are very efficient at removing gas from the ISM and slightly less efficient in removing gas from haloes. AGN lower the stellar mass fraction by a slightly smaller amount than it lowers the fraction of the mass in the ISM by redshift 2, as stellar mass also builds up in lower mass systems in which AGN feedback is less efficient. The stellar mass function, as shown in panel (I) slightly undershoots the observed stellar mass function. The SN feedback in this simulation was tuned to reproduce the total star formation rate density of the Universe fairly well. Including the extra AGN feedback will then under-reproduce the stellar mass content of the Universe.

2.11 Conclusions

We have analysed a large set of high-resolution cosmological simulations from the *OWLS* project (Schaye et al., 2010). We focused on the baryonic properties of (friends-of-friends) haloes at redshift 2, while varying parameters in the sub-grid models for radiative cooling, reionization, the pressure of the unresolved multi-phase ISM, star formation, stellar feedback and AGN feedback, as well as the cosmology, box size and mass resolution.

A central conclusion from this work is that the star formation rate is self-regulated by galactic winds driven by massive stars. The star formation rate adjusts so that the (time averaged) rate at which energy and momentum are injected is sufficient to balance the gas accretion rate. This self-regulation happens through the ejection of gas from the galaxy in large-scale outflows. For a fixed redshift and halo mass, the accretion rate is determined by cosmology and cooling. As the cooling rate is very sensitive to metallicity, chemical feedback is also important.

For low-mass haloes ($M \lesssim 10^{11}\,\mathrm{M}_\odot$, $M_* \lesssim 10^{9}\,\mathrm{M}_\odot$) the reheating associated with reionisation is important, although by $z = 2$ the results are insensitive to the redshift at which reionisation happened, at least as long as it happened no later than $z = 6$, as required by observations. Without reionisation, these haloes would host higher-mass galaxies with higher gas fractions.

For halo masses $M \gtrsim 10^{11}\,\mathrm{M}_\odot$ AGN feedback becomes significant and for $M \gtrsim 10^{12}\,\mathrm{M}_\odot$ ($M_* \gtrsim 10^{10}\,\mathrm{M}_\odot$) it strongly reduces the star formation rates and gas fractions. We note, however, that the mass for which AGN feedback becomes important can be changed by modifying the parameters of the black hole accretion model (Booth & Schaye, 2009). As was shown by Booth & Schaye (2009), AGN feedback self-regulates the growth of supermassive black holes through the ejection of gas from galaxies. As a result, the black hole growth rate adjusts so that the (time-averaged) rate at which energy and momentum are injected balances the rate at which gas accretes onto the galaxy. As the black hole regulates the gas fraction, it also regulates the star formation rate.

Conclusions that support this picture of self-regulated star formation and other conclusions from this work can be summarised as follows:

- The gas fractions of galaxies are sensitive to the assumed star formation law. If star formation is more efficient, the gas fraction is lower. This is a result of self-regulation: the gas fraction increases until the formation rate of massive stars is sufficient to drive galactic winds that can balance the rate at which gas accretes onto the galaxies. As a consequence, the star formation rates and stellar masses are insensitive to the assumed star formation law.

- In order for kinetic feedback to be efficient in suppressing star formation, the

initial wind velocity must exceed a minimum, halo mass dependent, velocity. As was also shown by Dalla Vecchia & Schaye (2008), if the wind speed is too low, the outflow is quenched by hydrodynamic drag in the ISM. As the pressure of the ISM increases with the mass of the galaxy, so does the required wind velocity. If the velocity is sufficiently high, then the mass loading factor sets the amount of mass removed from the system and hence the efficiency of the feedback.

- If winds do not escape the galaxies, the pile-up of newly created metals results in catastrophic cooling. The gas is efficiently converted into stars and gets exhausted. This results in a change in the relation between star formation rate and the mass of a galaxy. The SFR as a function of mass quickly becomes flatter because of the exhaustion of gas.

- The stellar mass, star formation rates, and gas fractions of galaxies are insensitive to the stiffness of the equation of state that we impose on the unresolved, multiphase ISM.

- In a cosmology with a higher σ_8 structure formation happens earlier, and therefore, galaxies in a fixed halo mass at a fixed time have somewhat higher stellar masses. The characteristic densities are also higher, which reflects the higher density of the Universe at the time the halo formed. These higher densities, in turn, cause feedback from star formation to become inefficient at slightly lower masses if σ_8 is higher. The differences in halo properties between different cosmologies are, however, much smaller than the differences between the cosmic star formation histories we found in Schaye et al. (2010). This is because the halo mass function is sensitive to cosmology, which is more important for the star formation history than the relatively small change in the internal properties of the galaxies at a fixed time and halo mass.

We compared our predictions to two different observational results: the specific star formation rate as a function of stellar mass and the stellar mass function. The latter function can be thought of as a convolution between the halo mass function and the stellar mass as a function of halo mass. As we are using the WMAP year-3 cosmology, our mass function is not quite right. In particular, our underestimate of σ_8 will cause us to underestimate the stellar mass function. Under the assumption that the difference in cosmology only affects the halo mass function, which is correct to first order (as our comparison of the WMAP year-1 and year-3 cosmologies confirms), we could correct our stellar mass function. We have not done this here, but plan to do so in future work.

The comparison with observations revealed that:

- In almost all simulations, the stellar mass function is close to the observed number densities of galaxies over much of the observed mass range. The shape is different though, with most models having a steeper low-mass end. None of the simulations predict a clear exponential cut-off at the high-mass end, but this could just be due to our limited box size (we plan to test this soon). The low-mass end is only steeper than extrapolations of Schechter-function fits to the observations. Except for models with inefficient feedback, the number densities agree well within the observed mass range.

- For a fixed wind energy per unit stellar mass, the slope of the low-mass end of the stellar mass function increases with the wind velocity. This is because higher wind velocities keep the feedback efficient up to higher masses. In addition, low wind velocities correspond to high mass loading factors and thus to more efficient feedback provided the wind velocity remains sufficiently high, as will be the case for lower mass galaxies. This suggests that we could reproduce a wide range of stellar mass functions by making the wind velocity a function of the halo mass, even for a fixed amount of energy.

- The predicted specific star formation rates as a function of stellar mass are lower than observed. The discrepancy is worst for models in which the feedback is efficient. The negative slope in the relation between the sSFR and stellar mass is only reproduced by models for which feedback is inefficient in the observed mass range. Models without any efficient feedback still underpredict the sSFRs because their stellar masses are high. The only models that can reproduce the high values of the observed sSFRs are those with very efficient feedback in low-mass galaxies (i.e. models with high mass loading factors) and these models still only match the observations for the stellar masses corresponding to the halo mass at which at the feedback is becoming inefficient. For higher stellar masses the sSFRs are again too low and the stellar mass function too high.

Thus, there is tension between the observed stellar mass function and the observed sSFRs. The high observed star formation rates are difficult to match unless feedback suddenly becomes inefficient at the lowest stellar masses for which observations are available ($M_* > 10^{9.5}\,\mathrm{M}_\odot$). It cannot be inefficient in low-mass progenitor haloes though, because otherwise the stellar mass would already be too high, which would reduce the sSFR and would overpredict the stellar mass function. The feedback can also not remain inefficient as the stellar mass increases or else the stellar mass function would again be too high.

Our investigation clearly shows that winds driven by feedback from star formation determine the main properties of galaxies residing in haloes of a given mass.

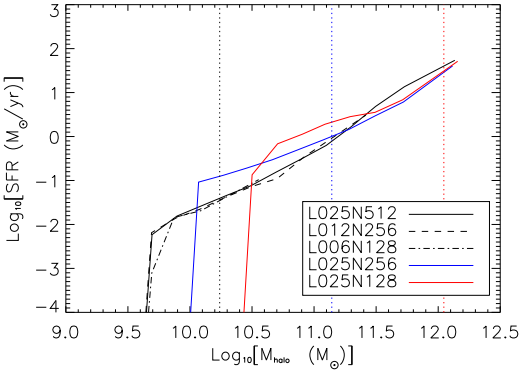

Figure 2.16: Median star formation rate as a function of halo mass at $z = 2$ for 5 simulations with different particle numbers and/or box sizes as indicated in the legend. The vertical dotted lines indicate the mass of 2000 dark matter particles in the simulations shown by the curves in the corresponding colours. At the low mass end, the median SFR falls to zero, as more than half of the haloes in a bin do not have gas particles with a density above the star formation threshold. Above a mass corresponding to 2000 dark matter particles per halo, the SFR as a function of halo mass is reasonably well resolved.

Even for a fixed amount of energy per unit stellar mass, variations in the subgrid implementation of feedback from star formation provide us with considerable freedom. This freedom can possibly be exploited to match observations spanning a wide range of masses, which would provide the simulations with some of the attractions of semi-analytic models. However, this potential success comes also with the disadvantages of such models: the underlying physics would remain poorly understood. As higher resolution simulations become feasible, the need for subgrid models to generate galactic outflows in cosmological simulations will hopefully be removed.

Further improvement in our understanding of the physics that determines the global properties of galaxies will likely come from theoretical models and observations focusing on galactic winds. The physics of star formation is less crucial as the time-averaged, galaxy-wide star formation rates are regulated by the large-scale outflows.

Acknowledgements

We kindly thank Danilo Marchesini for useful discussions about the observations of the stellar mass function and for providing his results in digital form. We furthermore are grateful to *OWLS* collaboration for useful discussions about and comments on this work. The simulations presented here were run on Stella, the LOFAR BlueGene/L system in Groningen and on the Cosmology Machine at the Institute for Computational Cosmology in Durham as part of the Virgo Consortium research programme.

Appendix A. Numerical convergence tests

In order to investigate the convergence of our results with respect to box size and resolution, the reference model is run in 5 different simulations, together making up complete sets of three simulations with the same box size, but different resolution and another set of three simulations with constant resolution but different box sizes. The simulation that is common to both, is the reference simulation used throughout the paper. We will denote the simulations as '*LXXXNYYY*', where *XXX* is the size of the simulation box in comoving h^{-1}Mpc and *YYY* is the number of particles per spatial dimension (for both dark matter and baryons we use YYY^3 particles). So, the reference simulation here is '*L025N512*'.

The two sets are:

- *L025N512*, *L012N256* and *L006N128*, which all have the same numerical resolution, but a different box size, varied in steps of a factor of two. These three runs will be shown in black lines with different line styles (solid, dashed and dot-dashed, respectively).

- *L025N512*, *L025N256* and *L025N128*, which have the same box size, but different resolutions. The mass and spatial resolutions change by a factor of 8 and 2, respectively. These will be shown by black, blue and red solid lines, respectively.

In this Appendix we will show all Friends-of-Friends haloes identified in the simulation that have at least 20 dark matter particles, which, as we will show, is not enough to obtain converged results.

Fig. 2.16 shows that the box size has no influence on the star formation rates, as the lines with different line styles (which corresponds to runs with the same resolution but different box sizes) all overlap. The only effect is in the sampling of the mass function: in a bigger box higher halo masses are sampled. This is as expected: the dense regions of haloes do not care about the size of the universe

one simulates (provided it is large compared with the objects themselves), but rare objects can only be sampled in sufficiently large boxes.

Mass resolution is an issue when simulating star formation, as can be seen by comparing the black, red and blue solid curves in Fig. 2.16. The minimum non-zero SFR a halo can have corresponds to having one star forming particle at the star formation threshold. For simulations with lower particle masses this minimum SFR is lower (the minimum SFR in the highest resolution simulation is $6.2 \times 10^{-4} = 10^{-3.2}\ M_{\odot}\ \mathrm{yr}^{-1}$ and scales linearly with particle mass). For the lowest halo masses for which the median star formation rates are non-zero, the SFR will be slightly overestimated. The overestimate results from the underestimate of the SFR at lower masses, which makes both gas consumption and gas removal through feedback less efficient. Because the lines all get close together at high masses, we conclude that the halo star formation rates converge at the high mass end. The unresolved star formation at early epochs (when a given halo is less massive) accounts for only a small fraction of the stellar mass in massive objects.

In Fig. 2.16 the vertical dotted lines denote 2000 times the dark matter particle mass in the simulations of the same colour. The halo star formation rates are reasonably converged above these halo masses, as can be seen by comparing the blue and black curves (highest versus eight times lower spatial resolution) to the right of the vertical blue dotted line. The halo mass regime where the median star formation rate is zero, because more than half the haloes do not have any gas particles with densities above the star formation threshold, is also removed when demanding a minimum number of 2000 dark matter particles per halo. The haloes are responsible for the sharp drop in the lowest mass bin.

The build-up of stellar mass is influenced by the SFR at all epochs prior to the epoch at which it is measured. As all haloes were initially small and thus poorly resolved, the early build up of stellar mass is underestimated. Indeed, Schaye et al. (2010) have already shown that our higher resolution simulations resolve the cosmic star formation rate at earlier epochs. We therefore expect that the convergence of the (s)SFR as a function of stellar mass is slightly worse than that of the SFR as a function of total halo mass.

Fig. 2.17 shows the same simulations as Fig. 2.16, but now we plot the specific star formation rate against halo stellar mass (SFR/M_{*}). The vertical cut-off at the low mass ends corresponds again to haloes for which the median star formation rate is zero. At slightly higher stellar masses the specific star formation rate decreases with stellar mass, but in this regime the results depend strongly on resolution. The same three regimes as in Fig. 2.16 can be identified, plus one additional effect: as the resolution is decreased, a fixed stellar mass corresponds to a smaller halo mass and hence a lower star formation rate. The mass range over which the sSFR is an increasing function of stellar mass starts at a stellar mass corresponding to

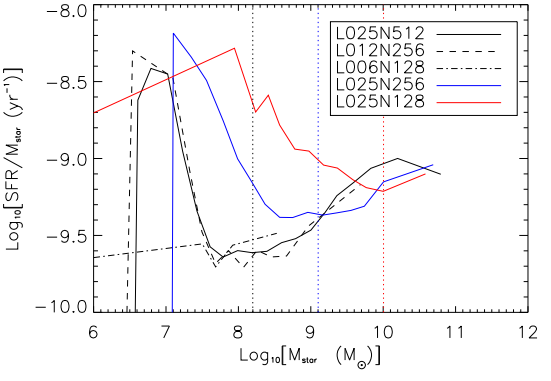

Figure 2.17: The median specific star formation rates of haloes as a function of their stellar mass at $z = 2$ for 5 simulations with different particle numbers and/or box sizes as indicated in the legend. The vertical dotted lines indicate the mass corresponding to 100 star particles in the simulations shown by the curves in the corresponding colours. The sharp cut-off at low masses again stems from the fact that there is a minimum to the (non-zero) SFR. Right of the vertical dotted lines the specific star formation rates are reasonably well converged.

about 100 star particles, as indicated by the vertical dotted lines. This is also the regime for which the results become insensitive to resolution, as can be seen by comparing the solid black and blue lines rightwards of the the blue, dotted line and by comparing the solid blue and red curves rightwards of the red, dotted line. We note that, as expected, the same trends are found for SFR/$M_{\rm gas}$.

Fig. 2.18 shows the stellar mass fraction as a function of halo mass for the same set of simulations as used in Fig. 2.16. The vertical dotted lines indicate our adopted resolution limit of 2000 dark matter particles. The diagonal dotted lines indicate the stellar mass fraction for haloes consisting of 100 star particles, which is our resolution limit for plots with stellar mass on the horizontal axis. The fact that for a given resolution (i.e. colour), the solid curve intersects the two dotted lines in nearly the same place, implies that the cuts of 100 star particles and 2000 dark matter particles are very comparable for the set of simulations of the reference model at high resolution. Above this resolution limit of 2000 dark matter particles, the stellar mass fractions are nearly converged. At lower resolution, a minimum number of dark matter particles is a more stringent cut than a minimum number of star particles. Throughout the paper we use a minimum number of dark matter particles when we plot quantities as a function of halo mass.

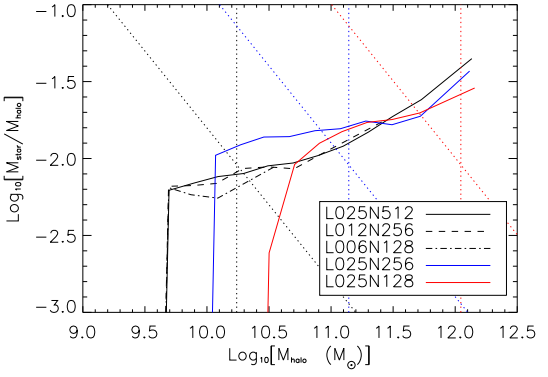

Figure 2.18: Median stellar mass fraction as a function of halo mass at $z = 2$ for 5 simulations with different particle numbers and/or box sizes as indicated in the legend. The vertical dotted lines indicate the mass corresponding to 2000 dark matter particles in the simulations shown by the curves in the corresponding colours. The diagonal black dotted line indicates the relation for haloes with 100 star particles (the cut that is made in the rest of the paper where relations with stellar mass are shown). As can be seen, in the highest resolution simulation, the cuts made throughout this paper in minimum number of dark matter particles and the minimum number of star particles roughly correspond to each other. At lower resolutions, the cut in dark matter particle number is more stringent.

Although we will not show them here, we found that stellar mass functions are already converged with respect to mass resolution for haloes with 10 star particles or more. Cuts in the number of dark matter particles, or in the total particle number, are much more delimiting. One would throw away many more haloes if a total particle number cut is made instead of a star particle number cut (the stellar mass function is only as nicely converged at $z = 2$ for haloes with 500 particles of all types together as it is for a minimum of 10 star particles). To be consistent with the rest of the results show in the paper, we only plot stellar mass functions for haloes with at least 100 star particles.

In general, every relation plotted in this paper demands its own particle number cuts for convergence. We find that 2000 dark matter particles or 100 star particles per halo results in good convergence for most of the quantities. These two cuts are therefore adapted throughout the paper. To avoid biasing the results, we impose a cut of 2000 dark matter particles when looking at relations with total halo mass and of 100 stars particles when investigating correlations with stellar mass.

Appendix B. The energy and momentum in momentum driven wind models

In this Appendix we will look in more detail into the energy and momentum injection in the 'momentum driven wind models', such as those used by Oppenheimer & Davé (2006, 2008) and in this work. Inspired by Murray et al. (2005), these models represent galactic winds which are driven by the radiation pressure from the galaxies' stellar population on the dust grains in the galactic outflows. As such, the amount of energy per unit stellar mass formed is not constant, but scales with galaxy mass as $E_w \propto M^{1/3}$. The total momentum used in the wind models is chosen so that the the total star formation rate density of the universe is fit, and is not restricted by what is actually available from SNe and radiation pressure.

Here, we will compare the momentum that goes into the wind, as compared to the momentum from the SNe themselves, as well as that resulting from the radiation pressure on the dust by the underlying stellar population. As default parameters for the SN ejecta we take that 10 $M_\odot$ of material is flowing out at a velocity of 3000 km s^{-1} (Murray et al., 2005). This sets both a kinetic energy and a momentum for this outflow.

For the radiation pressure, which results in an available momentum for the outflow, we will use the spectral synthesis models of Bruzual & Charlot (2003, (BC03)). We make the following assumptions:

1. Radiation is not scattered back and forth. In principle, from back-scattering a large gain in momentum can be obtained. We are talking here about stellar continuum radiation, which after the absorption by dust grains will be re-emitted at very long wavelengths, for which the optical depth is very low. The cross-section for this radiation to be back-scattered and be absorbed by another dust grain is very small. Only for extremely high physical densities, the shell that is driven will become optically thick for the thermal radiation of the dust grains. In that case, the diffusion of the photons outward may boost the momentum. This is a situation which can only be realized at the very early stages of driving the wind inside the molecular cloud, not at scales at which winds in the simulations are driven (~kpc).

2. All the radiation is used to drive an outflow. This, together with the previous point means that all the momentum in radiation is transferred to out flowing gas. Note that this is a very strong assumption, which makes the estimated outflow momentum from the radiation pressure an *upper limit*.

3. The driving radiation source is a simple stellar population of solar metallicity with a Chabrier (2003) IMF, the spectrum of which is well described by the

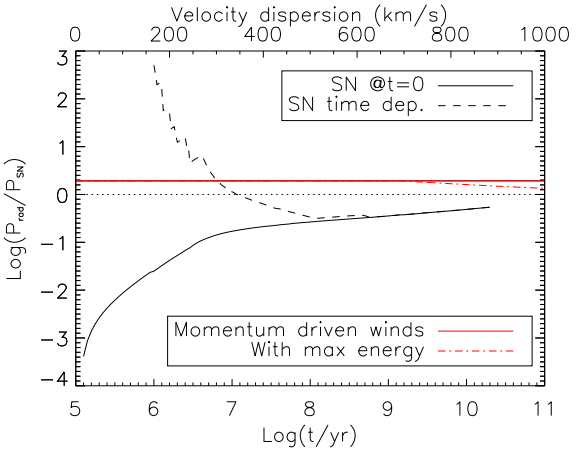

Figure 2.19: In black we show the ratio between the momentum available from radiation pressure and the momentum available from the supernova explosions themselves (assuming that 10 $M_\odot$ is ejected at 3000 km s^{-1} per supernova event). The solid black line assumes that all SNe go off at $t = 0$, so it is the integral of the radiation pressure as a function of SSP age, normalized by the total momentum in SNe. The dashed line instead has the momentum from radiation normalized to the total momentum from SNe up to that age. In red we show the amount of momentum that is put into the winds in the momentum driven wind simulations. The ratio between the red line solid line and the black dashed line (about an order of magnitude at $t = 10^7$ yr) is therefore the factor by which the momentum is boosted in the simulations compared to what comes from radiation. The top horizontal axis refers to the red dot-dashed line, which shows the momentum in winds in the model of Oppenheimer & Davé (2008), where the energy in the winds is limited to 2 times the energy available from SNe. This only becomes a small correction at velocity dispersions greater than 700 km s^{-1}. As the momentum from radiation is an upper limit, it is clear that the amount of momentum in the winds in the momentum driven wind simulations is unrealistically high.

high resolution spectra of the BC03 set of spectra for all ages.

In a time interval Δt, during which the source has luminosity L, the energy and momentum that the radiation can transfer to the gas are $E_{rad} = L \cdot \Delta t$ and $p_{rad} = L \cdot \Delta t/c$, respectively, where c is the speed of light.

In Fig.2.19 we show, as a function of age of the SSP, the total momentum the radiation can have transferred to the out flowing gas, up to that age. This value is normalized by the total amount of SN momentum, assuming the mass and velocity given above. The solid black line is under the assumption that all SNe go off at $t = 0$ (so normalized to the total available momentum from supernovae that result from the SSP), while the dashed black line follows the timed SN explosions (for all of which the same momentum is taken). This timed release is estimated from the number of neutron stars and black holes present in the sample according to the BC03 package. This adds up to the same number of SNe at the age where the lines meet ($t =\sim 10^8$ yr). The red lines in the plot show the amount of momentum that is used in the simulations described in the paper. The solid horizontal line shows the momentum that is used in all momentum-driven wind models described in this paper. The model used in Oppenheimer & Davé (2008) limits the energy in the winds to be two times the energy available from SNe, which results in the red dot-dashed line, in haloes with velocity dispersions as shown on the top horizontal axis. This maximum to the energy makes little difference, and no difference in haloes of velocity dispersion lower than 700 km s^{-1}.

From Fig.2.19 we learn that the amount of momentum available from radiation is, even after the entire 20 Gyr lifetime of the SSP still falls short by a factor of a few, compared to the total momentum in the SN ejecta. Remember that the momentum from radiation is an upper limit. At the time all SNe just went off, there is a factor 7 difference between the two.